14

Creep Behaviors and Influence Factors of FGH95 Nickel-Base Superalloy

Tian Sugui and Xie Jun
Shenyang University of Technology
China

1. Introduction

With the development of aerospace and ground transportation industry, the properties of aerospace engine are increasingly required to be improved. And especially, Turbine disk is one of the important component parts for advanced aero-engines, serving usually in the condition of 540～840°C at higher stress, so the turbine disks are required to be of high temperature tolerance and creep resistance (Flageolet B. et al., 2005; Liu D. M. et al., 2006). Thereinto, the continuous plastic flow of a material during creep can eventually result in large plastic deformations and significant modifications to the microstructure of the material, so that occurs the creep fracture of the turbine disk parts. Therefore, it is very important for the aero-engine materials to have a better property of the creep resistance.

Traditional wrought superalloys can hardly meet the requirements of the turbine disks in the advanced aerospace for their poor temperature tolerance and loading capacity resulted from their serious composition segregation in ingots and poor hot processability (Park N. K. & Kim I. S., 2001; Lherbier L. W. & Kent W. B., 1990; S. Terzi et al., 2008), especially the weaker cohesive force of grain boundaries (Paul L., 1988; Wang P. et al., 2008; Jia CH. CH. et al., 2006). While nickel based powder superalloys are an excellent material used for preparing the high temperature rotating section of the advanced aero-engine because its advantages are no macro-segregation in the ingot, chemical composition uniformity and high yield strength (Lu Z. Z. et al., 2005; Zhou J. B. et al., 2002).

FGH95 alloy is a nickel-base powder superalloy in which microstructure consists of γ matrix, γ' and carbide phases. The characteristics of FGH95 superalloy include the high extent of alloying and high volume fraction of γ'-phase (about 50%), besides the alloy possesses excellent integrating mechanical properties at 650°C (Domingue J. A., et al. 1980; Hu B. F. et al., 2006). Moreover, various size, morphology and distribution of γ' phase in the alloy can be obtained by different heat treatment regimes (Zainul H. D., 2007). The preparation technologies of FGH95 superalloy includes the powder pretreatment, hot isostatic pressing (HIP) and heat treatment. The heat treatment regimes of the alloy include the high temperature solution and twice aging treatment. After solution treated at high temperature, the alloy may adopt the different cooling methods, such as cooled in molten salt or in oil bath, and the microstructure and creep properties of the alloy are related to the chosen heat treatment regimes (Klepser C. A., 1995).

The deformation mechanism of the polycrystalline Ni-base superalloys during creep includes twinning, dislocations by-passing or shearing into the γ′ phase (Raujol S. et al., 2004 ; Kovarik L. et al., 2009). Actually, the mechanical properties and creep behaviors of the alloy are related to the quantities, morphology and distribution of γ′-phase, and especially, the configuration of the boundary and carbides have an important effect on the creep resistance of the alloy (Viswanathan G. B. et al., 2005; Hu B. F. et al., 2003). For example, after the alloy is solution treated for cooling in molten salt, the total number and size of secondary γ′ phase increase, which can effectively improve the plasticity of the alloy at high temperature (Zhang Y. W. et al., 2002). Because the various microstructures in the alloy may be obtained by different heat treatment regimes, it is very important to understand the influence of heat treatment regimes on the microstructure and creep resistance of the alloy.

In this chapter, the different HIP alloys are solution treated at different temperatures, and cooled in the molten salt or oil bath, respectively, then through twice aging treatment. Besides, some full heat treated alloys are aged for different time at high temperatures, and then the parameters of γ′, γ phases in the alloy are measured for evaluating the effect of the long term aging time on the misfits. The creep properties of the alloy treated by different heat treated regimes are measured under the conditions of the applied different temperatures and stresses, and the microstructures of the alloy are observed by using SEM and TEM for investigating the influences of the heat treatment regimes on the microstructure and creep properties. Additionally, the deformation mechanism and fracture feature of the alloy during creep are briefly discussed.

2. Experimental procedure

FGH95 powder particles of the nickel-base superalloy with the size of about 150 meshes were put into a stainless steel can for pre-treating at 1050 °C for 4 h. The can containing FGH95 powder alloy was hot isostatic pressed (HIP) for 4 h under the applied stress of 120 MPa at 1120 °C, 1150 °C and 1180 °C, respectively. The heat treatment and long term aged treatment regimes of the alloy are listed, respectively, in the Table 2.1 and Table 2.2. The cooled rates of the specimen in the oil bath and molten salt are measured to be about 205 °C/min and 110 °C/min, respectively. The error ranges of the used heating furnace are about ± 2 °C. The chemical composition of FGH95 superalloy is shown in Table 2.3.

HIP Temp., (°C)	Solution Temp., (°C)	Quenching Temp., (°C)	Double aging treatment
1120	1140 for 1 h 1150 for 1 h 1160 for 1 h 1165 for 1 h	cooled for 15 min in molten salt at 583 °C	870 °C×1h + 650 °C×24h
1180	1150 for 1 h 1160 for 1 h	cooled for 15 min in oil bath at 120 °C	
	1150 for 1 h 1160 for 1 h	cooled for 15 min in molten salt at 583 °C	

Table 2.1. Heat treatment regime of FGH95 superalloy

HIP Temp., (°C)	Heat treatment	Aging regime
1120	1155 for 1 h + cooled for 15 min in molten salt at 550 °C + 870 °C×1h +650 °C×24 h	450 °C×500 h 450 °C×1000 h 550 °C×500 h 550 °C×1000 h
1150 1180		----

Table 2.2. Long time aging treated regime of FGH95 superalloy

C	B	Cr	Co	Al	Ti	W	Mo	Nb	Ni
0.060	0.012	12.98	8.00	3.48	2.55	3.40	3.40	3.50	Bal

Table 2.3. Composition of FGH95 superalloy（mass fraction,%）

By means of the anode selective dissolving method, the volume fraction of γ′-phase in FGH95 alloy was measured to be about 47%. Thereinto, the electrolytic extraction of γ′ phase in the alloy was conducted for separating from the γ matrix under the condition of the temperature at 0°C and current density about 50mA/cm^2. The choosing electrolyte solution consisted of $(NH4)_2SO_4$ and citric acid, the experimental device of the electrolytic extraction was shown in Fig. 2.1. After the electrolytic extraction was conducted, the granularity distribution, phases constituting and the misfit of γ′, γ phases in the alloy were measured by means of the XRD analysis and SEM/EDS observation.

The ingot of FGH95 superalloy was cut into the specimens with the cross-section of 4.5 mm × 2.5 mm and the gauge length of 20 mm, and the size of the sample was shown in Fig. 2.2. Uniaxial constant load tensile testing was performed, in a GWT504 model creep testing machine, for measuring creep curves under the experimental conditions of 984 MPa ~ 1050 MPa and 630 °C ~ 670 °C. The yield strength of FGH95 alloy was measured to be 1110 MPa at 650 °C. The strain data of the alloy at different conditions were measured with an extensometer to portray the creep curves, twice of the each creep testing were conducted for ensuring the statistical confidence. The specimens of FGH95 alloy at different states were grinded and polished for observing the microstructure by using SEM and TEM, so that the influence of the heat treatment technics on the microstructure, the creep feature and fracture mechanism of the alloy was investigated.

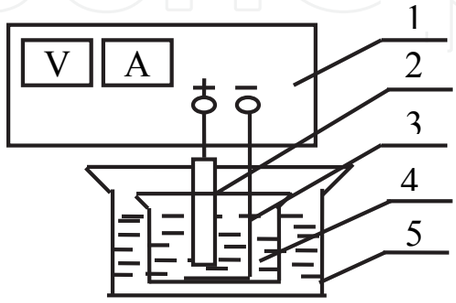

Fig. 2.1. Experimental equipment
1--Power supply, 2--sample, 3-- cathode, 4--solution, 5--container

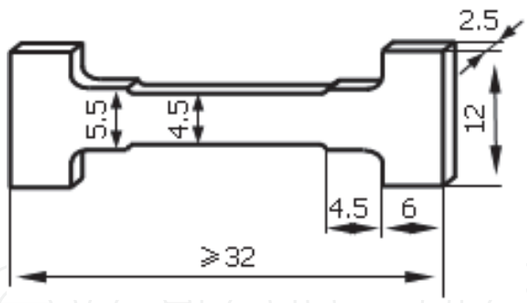

Fig. 2.2. Schematic diagram of the tensile creep sample

3. Influence of HIP temperatures on microstructure

3.1 Influence of HIP temperatures on microstructure of FGH95 alloys

After the alloy was hot isostatic pressed at different temperatures, the microstructure of the HIP alloys was shown in Fig. 3.1. The regions which were encompassed by coarse γ′ phase were defined as previous powder particles. After 1120 °C hot isostatic pressing molded, the alloy consisted of γ′ and γ phases, thereinto, the coarser γ′ phase distributed around the powder particles was defined as the previous particle boundaries (PPB). Therefore, the configuration of sphere-like previous particle was clearly appeared, and the power particle size was about 15~25 μm, as shown in Fig. 3.1(a).

With the HIP temperature increased to 1150 °C, the size of the powder particles was similar to the former, but the sphere-like configuration was not clearly. The PPBs consisted mainly of the coarse γ′ phase, and the size and amount of the coarser γ′ phase decreased slightly as shown in Fig. 3.1(b). As the HIP temperature increased to 1180 °C, the size of the grain grew up obviously, being about 20~40 μm. Besides, the grain boundaries appeared the straight-like feature, and the amount and size of the coarse γ′ phase decreased obviously as shown in Fig. 3.1(c). The dark regions around the powder particles were defined as the previous particle boundaries (PPB) in which the secondary γ′ phase was precipitated along the different orientations as marked by letters A and B.

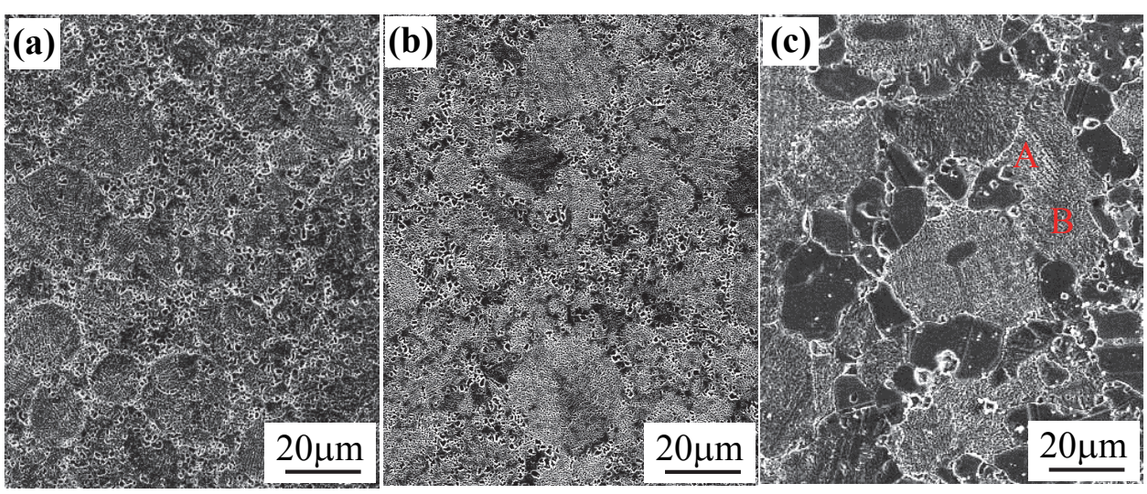

Fig. 3.1. Microstructure of the alloy after HIP treated at different temperatures.
(a) 1120 °C,(b) 1150 °C,(c) 1180 °C

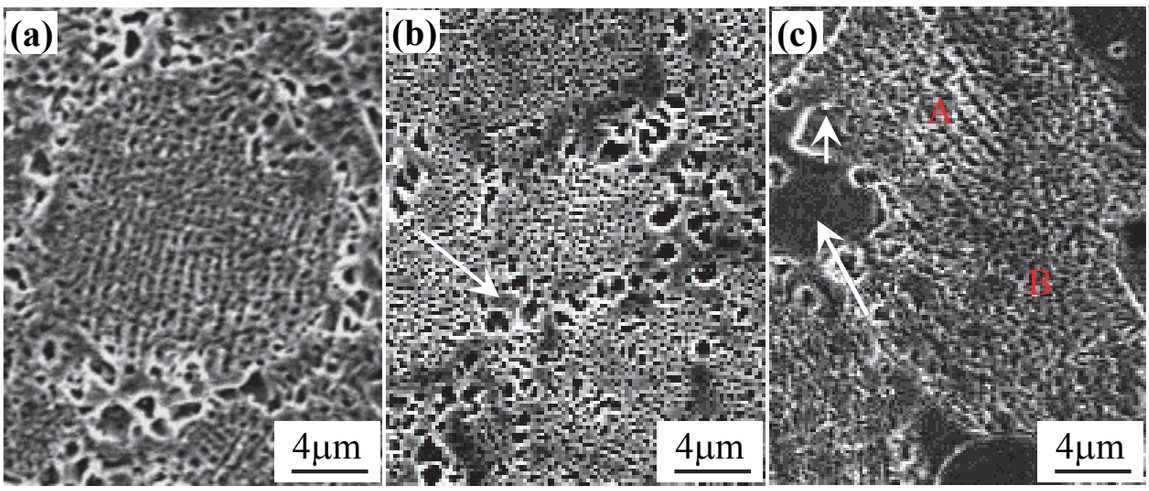

Fig. 3.2. Magnified morphology of the alloy HIP treated at different temperatures. (a) finer γ′-phase precipitated within the grain of the alloy treated by HIP at 1120 °C, (b) after HIP treated at 1150 °C, no γ′- phase particles precipitated in the regions near the coarser γ′-phase as marked by arrow, (c) after the alloy treated by HIP at 1180 °C, particle-like carbides precipitated along the boundary as marked by short arrow.

The magnified morphology of the alloys which were hot isostatic pressed at different temperatures was shown in Fig. 3.2. Thereinto, the γ′ phase displayed the black color due to the dissolved during chemical corrosion, and the γ matrix which is not dissolved displays the gray color. After HIP treated at 1120 °C, the coarser γ′ phase which distributed around the PPB was about 1~2 μm in size and was defined as the primary γ′ phase. Besides, the fine secondary γ′ phase was regularly distributed along the same orientation within the previous powder particles as shown in Fig. 3.2(b). As the HIP temperature increased to 1150 °C, the secondary γ′ phase about 0.1~0.3 μm in size was dispersedly precipitated within the grain, and the coarser γ′ phase still existed in the PPB regions. Moreover, the depleted zone of the fine γ′-phase appeared in the regions near the coarser γ′ phase, as marked by the arrow in Fig. 3.2(b).

The magnified morphology of the powder particle in the 1180 °C HIP alloy was shown in Fig. 3.2(c), indicating that the fine secondary γ′ particles with different orientations were precipitated within the same grain as marked by A and B in Fig. 3.2(c). No fine γ′ particles were precipitated in the PPB regions near the coarser γ′ phase, so the region was defined as the depleted zone of the fine γ′-phase as marked by the long arrow in Fig. 3.2(c). Moreover, some white carbide particles were precipitated in the PPB region as marked with the white short arrow in Fig. 3.2(c).

The microstructure of the different temperature HIP alloys which were solution treated at 1155 °C, cooled in the molten salt at 520 °C and twice aging treated was shown in Fig. 3.3. The microstructure of the 1120 °C HIP alloy after full heat treated was shown in Fig. 3.3(a), illustrating that a few of coarser γ′ phase was distributed along the grain boundaries. And the size of the coarse γ′ phase was about 1 ~ 2 μm, as marked with the white short arrow in Fig. 3.3(a). Besides, the fine γ′ phase was dispersedly precipitated within the grain as marked with the long arrow in Fig. 3.3(a). Comparing to Fig. 3.3(a), the microstructure of the 1150 °C HIP after full heat treatment had no obvious distinction to the former, and the grain size

was about 10~25μm. The secondary γ′ phase was dispersedly distributed in the alloy as shown in Fig. 3.3(b). With the HIP temperature increased to 1180 °C and after full heat treatment, the PPB trace was kept in the alloy as marked with the long arrow in Fig. 3.3(c), indicating that the grain grew up obviously after HIP treated at 1180 °C, and the coarse γ′ phase dissolved completely, only kept a few of primary γ′ phase which size was about 1μm in the grain boundaries as marked with the short arrow in Fig. 3.3(c). Moreover, some fine carbide particles were dispersedly precipitated in the alloy as shown in Fig. 3.3(c).

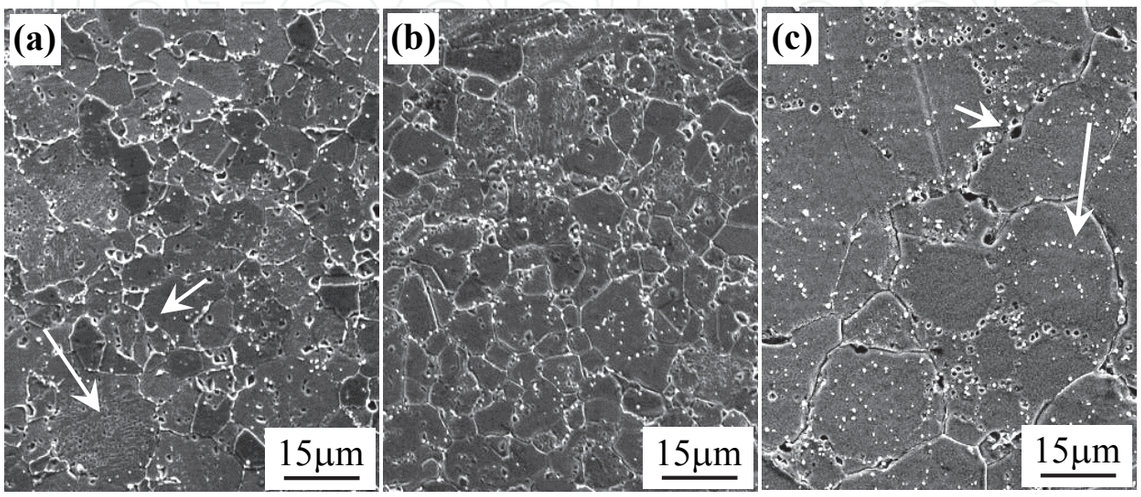

Fig. 3.3. Microstructure of the different temperatures HIP alloy after fully heat treated.
(a) 1120 °C, (b) 1150 °C, (c) 1180 °C

The magnified morphology of the different temperature HIP alloy after fully heat treated was shown Fig. 3.4. After the 1120 °C and 1150 °C HIP alloys were fully heat treated, a few of coarse γ′ phase was precipitated along the boundary regions as marked with short arrow in Fig. 3.4(a) and (b). And the coarse γ′ phase appeared in the boundary as shown in Fig. 3.4(a).

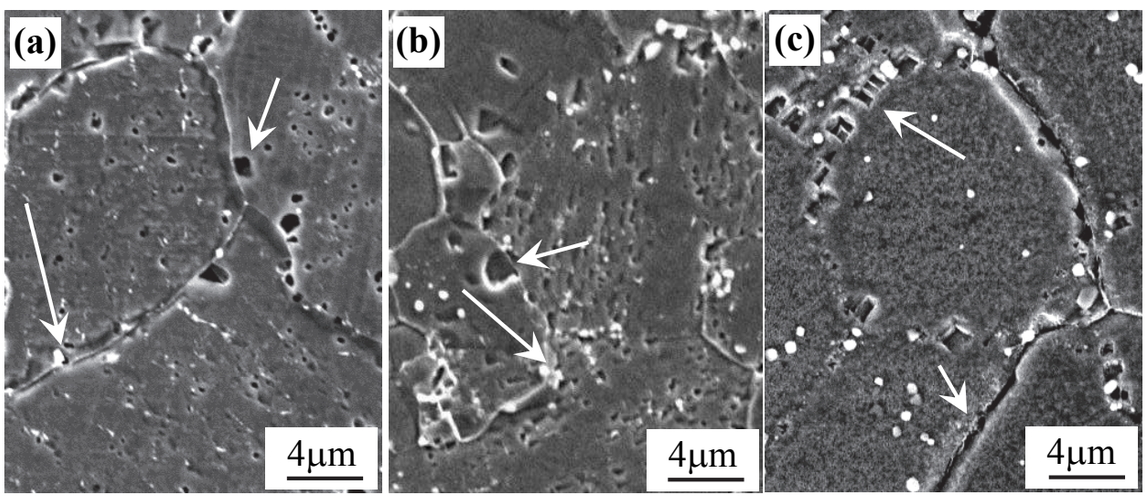

Fig. 3.4. Magnified morphology of the different temperature HIP alloy after fully heat treated (a) 1120 °C, (b) 1150 °C, (c) 1180 °C

Moreover, fine white particles were discontinuously precipitated along the boundaries as marked with the long arrow in Fig. 3.4(a) and (b), and the fine secondary γ′ phase and white particles were dispersedly distributed in the alloy as shown in Fig. 3.4(a) and (b). With the HIP temperature increased to 1180 °C and after fully heat treated, the sphere-like PPB kept in the alloy as marked with long arrow in Fig. 3.4(c), and the boundaries displayed an obvious straight feature as marked with short arrow in Fig. 3.4(c). Moreover, fine γ′ phase was dispersedly distributed within the grain, and the white particles of about 0.2 μm in size were dispersedly precipitated in the grain as shown in Fig. 3.4(c).

3.2 Analysis on the influence of HIP temperatures on microstructure

When the FGH95 alloy was HIP treated at 1120 °C and 1150 °C which is lower than the dissolving temperature of γ′ phase (T_m= 1160 °C), the coarse γ′ phase distributed around the PPB were not completely dissolved. Therefore, the γ′ phase which was reserved in the PPB regions was going to grow up during the slowly cooling stage of HIP, which resulted in forming the morphology of the coarser γ′ particles distributed along the PPB. The size of previous powder particles were kept in the alloy because no enough deformed energy which come from the HIP deformation promoted the powder particles growth up, as shown in Fig. 3.1(a) and (b).

When the alloy was hot isostatic pressed under the conditions of 120 MPa at 1180 °C, the coarser γ′ phase in the PPB regions was completely dissolved, which may enhance the diffusion rate of the elements and reduce the transferring resistance of the boundaries to promote the growth of the grain, therefore, the alloy displayed a larger grain size as shown in Fig. 3.1(c). At the same time, the nucleation and growth of the carbide occurred on the fine oxides which existed in the powder particle surface, and the carbide nucleation process only needs lower energy (Domingue J. A. et al., 1980). Consequently, some white carbide and coarser γ′ particles were discontinuously precipitated in the PPB regions as shown in Fig. 3.2(c), and the depleted zones of the fine γ′ phase appeared in the region near the coarse γ′ particles, due to the coarsening of γ′ particles to consume the much more elements of γ′ former, as shown in Fig. 3.2(c).

4. Influence of solution temperatures on microstructure

4.1 Influence of solution temperature on the microstructure

After the 1120 °C HIP alloy was solution treated at 1140 °C and twice aged, the grain size of the alloy was homogeneous, and fine γ′ phase was dispersedly precipitated within the grain, as shown in Fig. 4.1(a). Besides, much more coarse γ′ phase precipitated along the grain boundaries as marked with the arrow in Fig. 4.1(a). The magnified morphology was shown in Fig. 4.1(b), significant amount of fine γ′ phase were dispersedly distributed in the alloy, and the depleted zone of γ′-phase appeared around the coarse γ′ phase which distributed along the boundary regions, as shown in the Fig. 4.1(b).

With the solution temperature increased to 1150 °C, the microstructure of the alloy consisted of the γ′ and γ phases, the average grain size of the alloy was about 10~20 μm, as shown in Fig. 4.2(a), which indicated that some coarser γ′-particles are precipitated in the wider boundary regions, and the average size of the coarser γ′ phase was about 1~2.5 μm. The magnified morphology of the alloy was shown in Fig. 4.2(b), indicating that significant amount of the fine γ′ particles were dispersedly distributed within the grains, the size of the

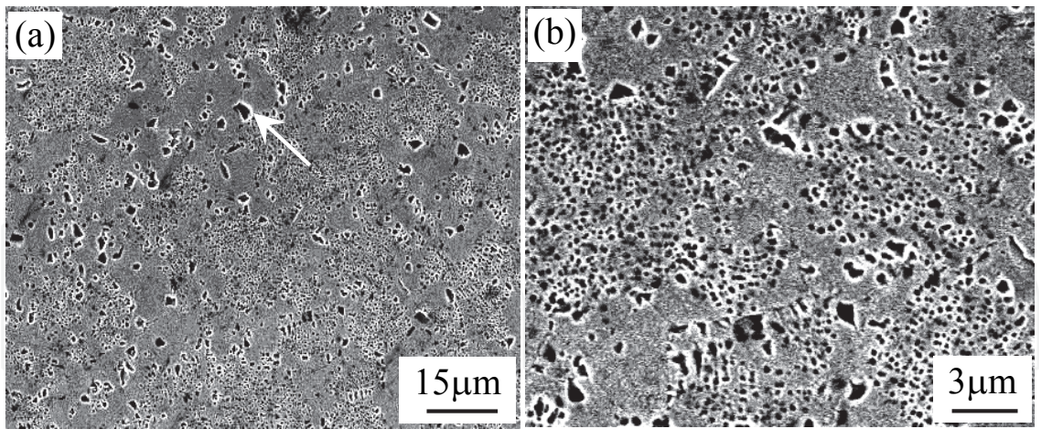

Fig. 4.1. Microstructure of the alloy after solution treated at 1140 °C. (a) after solution treated at 1140 °C, coarse γ′ phase distributed in the alloy, (b) no finer γ′ phase precipitated in the regions near the coarser γ′ phase

ones was about 0.1~0.3 μm. And no fine γ′-particles were precipitated in the regions near the coarser γ′-phase, the regions were defined as the depleted zone of the fine γ′-phase as marked by the arrow in Fig. 4.2(b), the magnified morphology of the depleted zone of γ′-phase was marked by the arrow in Fig. 4.2(c).

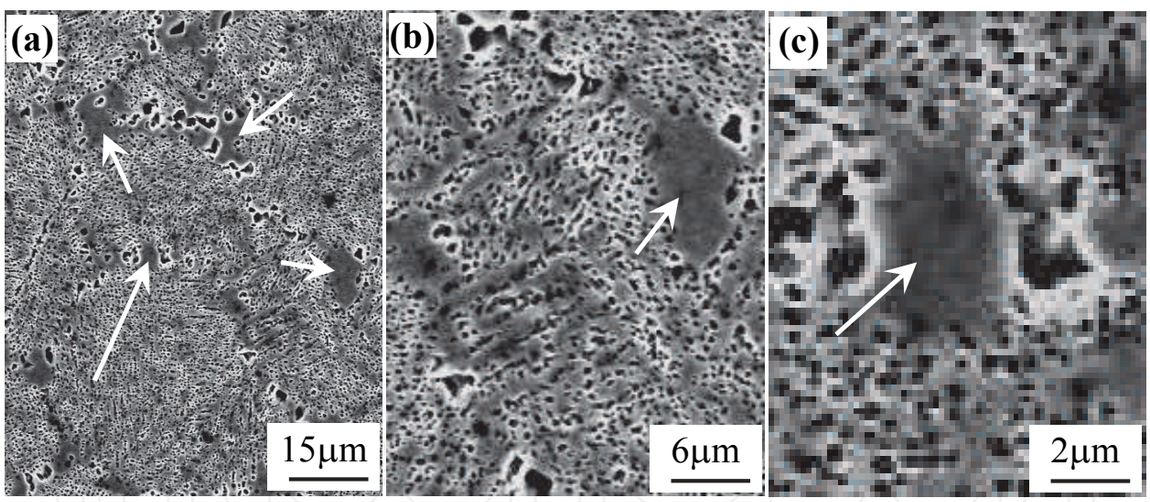

Fig. 4.2. Microstructure of the alloy after solution treated at 1150 °C. (a) After solution treated at 1150 °C, some coarser γ′ phase precipitated in the wider boundary regions, (b) fine γ′ phase distributed dispersedly within the grains, and the depleted zones of the fine γ′ phase marked by arrow, (c) magnified morphology of the depleted zone of γ′-phase

As the solution temperature increased to 1160 °C, the grain boundaries appeared obviously, and the average size of the grains in the alloy was about 15 ~ 25 μm as shown in Fig. 4.3(a). Compared to Fig. 4.2(a), the coarser γ′-precipitates in the boundary regions disappeared, and the white particles with size about 0.2 μm were precipitated within the grains and along the boundaries as marked by the arrows in Fig. 4.3(a). The magnified morphology of the alloy was shown in Fig. 4.3(b), indicating that the coarser γ′ particles and depleted zone of the fine

γ′ phase had disappeared, and the secondary γ′ phase was dispersedly distributed within the grains. The grain boundary in the alloy was marked by longer arrow and some particles were homogeneously precipitated along the boundaries and within the grains as marked by the short arrows in Fig. 4.3(b).

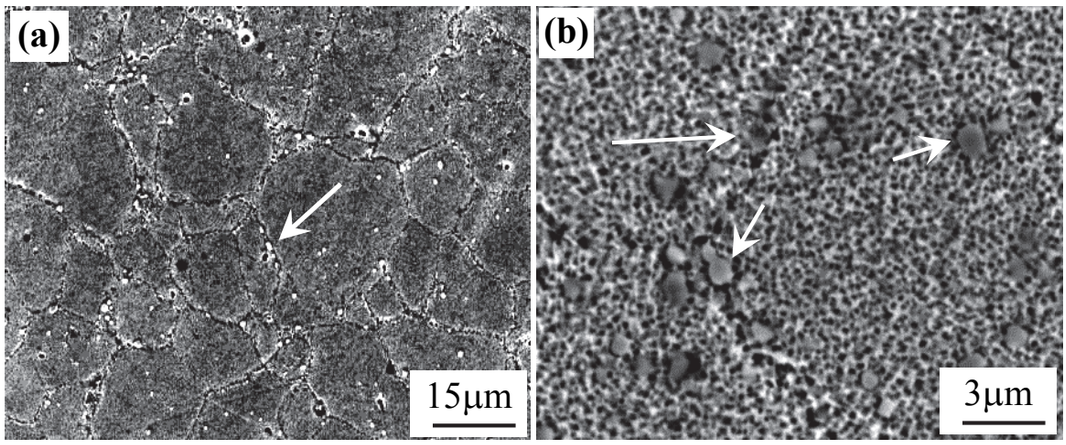

Fig. 4.3. Microstructure of the alloy after solution treated at 1160 °C. (a) after solution treated at 1160 °C, the coarser γ′ phase disappearing and the grain boundaries appearing obviously in the alloy, (b) the secondary γ′ phase distributed dispersedly within the grain, and some particles precipitated in the alloy as marked by the arrows

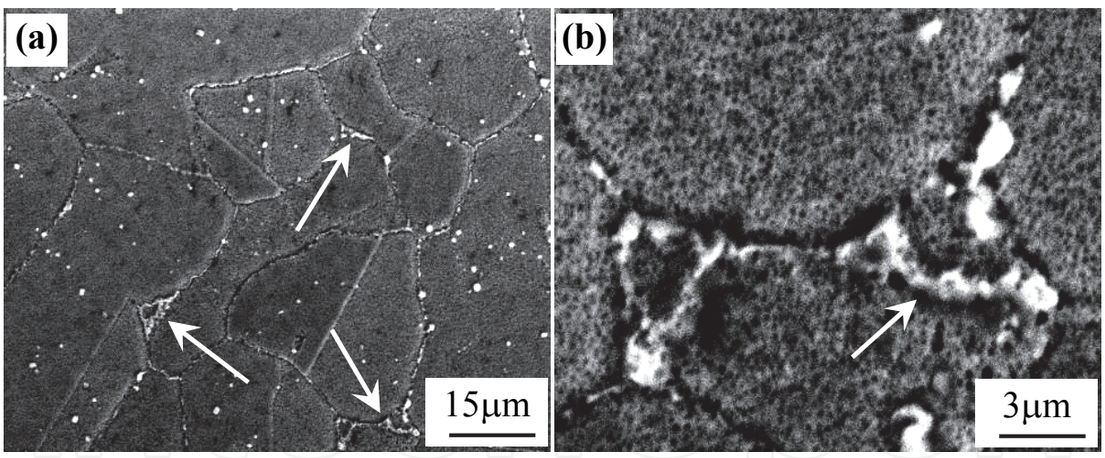

Fig. 4.4. Microstructure of the alloy after solution treated at 1165 °C. (a) After solution treated at 1165 °C, the average size of the grains in the alloy increasing obviously, and films of white phase precipitated along the boundaries as marked by arrows, (b) the secondary γ′ phase distributed dispersedly within the grains, and films of the white phase distributed along the grain boundaries

As the solution temperature increased to 1165 °C, the grain sizes in the alloy increased, the linear-like boundaries appeared in the alloy, and the films of the white phase were continuously precipitated along the boundaries as marked by the arrows in Fig. 4.4(a). The magnified morphology of the white phase was shown in Fig. 4.4(b), indicating that white particles were continuous precipitated to form the films along the boundaries as marked by

the arrow in Fig. 4.4(b), and significant amount of the fine secondary γ′ phase were precipitated within the grains, no depleted zones of the fine γ′ phase were detected in the alloy. The grain sizes after the alloy was solution treated at various temperatures were measured as listed in Table 4.1. Moreover, by means of composition analysis under SEM/EDS, it is indicated that the elements Nb, Ti and C are richer in the white particles which were located within the grain and boundary regions as shown in Fig. 4.3 and Fig. 4.4, respectively.

After the alloy was solution treated at 1160 °C, the fine γ′-particles with the size of about 0.1 μm were dispersedly precipitated within the grains as shown in Fig. 4.5(a), the particles can effectively hinder the dislocation movement to enhance the creep resistance of the alloy. The smaller space between the fine γ′-particle was measured to be about 0.03 μm, the bigger space between the fine γ′-particles is measured to be about 0.12 μm as marked by letters L_1 and L_2 in Fig. 4.5(a), respectively. It was indicated by TEM/EDS analysis that the elements Nb, Ti and C richer in the carbide particle which was located in the boundary as shown in Fig. 4.5(b), and the particle was identified as (Nb, Ti)C phase by means of the diffraction spots analysis as marked in Fig. 4.5(c).

Solution temp. (°C)	1140	1150	1160	1165
Average grain sizes (μm)	10~20	10~20	15~25	20~40

Table 4.1. Grain sizes of the alloy solution treated at different temperatures

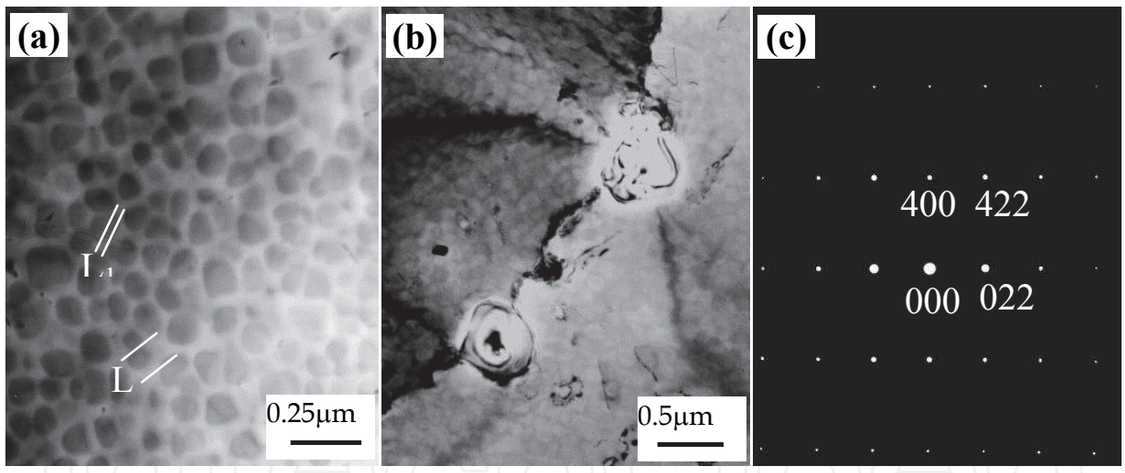

Fig. 4.5. Morphologies of γ′ and carbide phases. (a) Fine γ′ phase precipitated dispersedly within the grain, (b) carbide particles precipitated along the boundaries, (c) SAD patterns

4.2 Influence of quenching method on the microstructure

After the 1180 °C HIP alloy was solution treated at different temperatures and cooled in oil bath at 120 °C and twice aging treated, the alloy displayed the various sizes of grains in which the fine γ′ phase was dispersedly and regularly precipitated, as marked by white long arrow in Fig. 4.6(a). The bigger grains was about 40~60 μm in size, the smaller grains was about 20 μm in size, the bunch-like coarser γ′ particles were distributed in the PPB regions, or some coarser γ′ particles were congregated in the local regions as marked by black arrow in Fig. 4.6(a). The depleted zone of the fine γ′-phase appeared in the regions near the coarser γ′ phase as marked with the white short arrow in Fig. 4.6(a). As the solution temperature

increased to 1160 °C, the coarser γ′ phase in the alloy was completely dissolved due to the higher solution temperature. Moreover, the fine γ′ phase and the white particles were dispersedly distributed within the grains, respectively, and some white particles were precipitated along the boundaries as marked by white arrow in Fig. 4.6(b). Furthermore, the twinning appeared within the grain as marked by black arrow in Fig. 4.6(b).

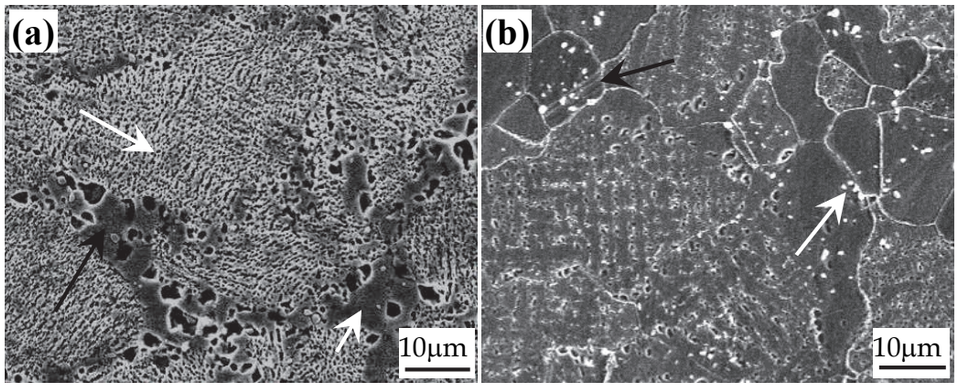

Fig. 4.6. Morphology of the alloy after solution treated at different temperatures and cooled in oil bath. (a) After solution treated at 1150 °C, the fine γ′ phase distributed dispersedly within the grains, and the depleted zone of γ′-phase as marked by shorter arrow. (b) after solution treated at 1160 °C, the fine γ′ phase and carbide particles distributed dispersedly within the grains, respectively

After solution treated at 1150 °C, then cooled in molten salt and twice aged, the microstructure of the alloy consisted of the particle-like γ′phase with different size, the coarser γ′-phase was distributed in the PPB regions as marked by white arrow, and the fine γ′ phase was dispersedly distributed within the grain as marked by black arrow in Fig. 4.7(a). Furthermore, the depleted zone of the fine γ′ phase appeared in the region near the coarser γ′-phase as marked by white short arrow in Fig. 4.7(a), and the size of the fine γ′ phase was about 0.15 μm.

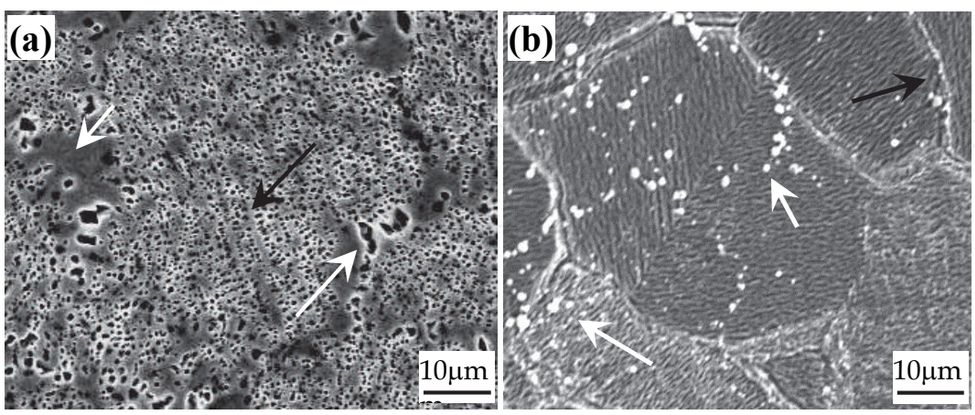

Fig. 4.7. Morphology of the alloy after solution treated at different temperatures, and cooled in molten salt. (a) After solution treated at 1150 °C, the fine γ′ phase distributed dispersedly in the grains, and the coarse γ′ particles precipitated along the boundaries, (b) after solution treated at 1160 °C, straight-like boundaries marked by black arrow, and the fine particles distributed dispersedly within the grains.

5. Influence of aging time on microstructure and misfits

5.1 Influence of aging time on microstructure

After the 1120 °C HIP alloy was solution treated at 1155 °C, cooled in molten salt at 520 °C and twice aging treated, the microstructure of the full treated alloys which were kept at 450 °C and 550 °C for 500 h respectively was shown in Fig. 5.1(a) and (b). Compared to the alloy which was not long time aged, no obvious distinction on the microstructure was detected in the alloy which was long time aged for 500 h at 450 °C, as shown in Fig. 5.1(a). Thereinto, no obvious change on the grain size was found, and a few coarse γ′ particles about 1~2 μm in size was precipitated along the boundaries as shown in the Fig. 5.1(a). With the long time aging temperature increased to 550 °C, the grain size about 15~20 μm was similar to the former, and some coarse γ′ phase were distributed along the boundaries as shown in Fig. 5.1(b).

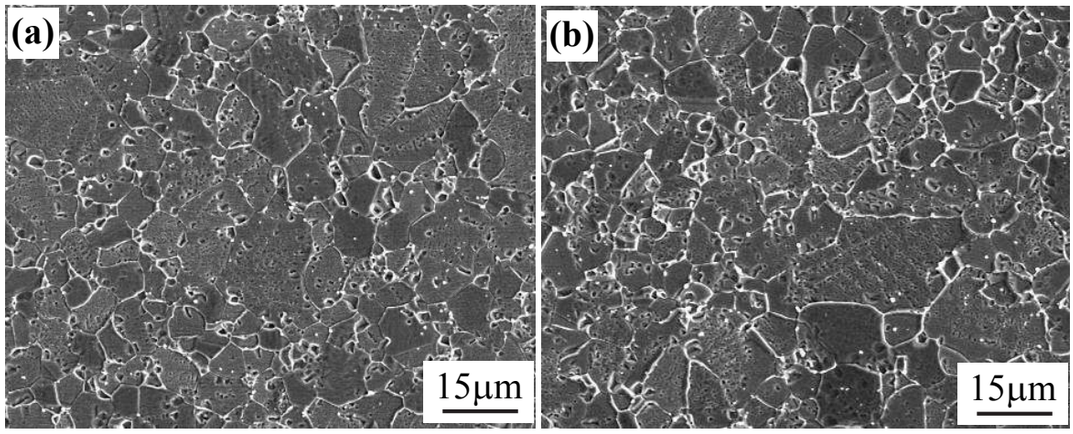

Fig. 5.1. Microstructure of the alloy aged for 500 h at different temperatures. (a) 450 °C, (b) 550 °C

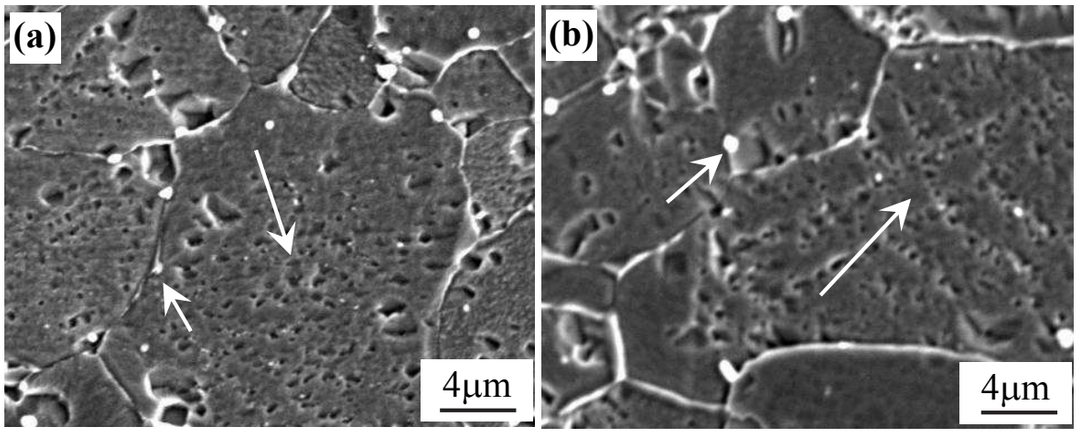

Fig. 5.2. Magnified morphology of the alloy aged for 500 h at different temperatures. (a) 450 °C, (b) 550 °C

The magnified morphology of the alloys aged for 500 h at 450 °C and 550 °C was shown in Fig. 5.2(a) and (b), respectively. After the alloy aged for 500 h at 450 °C, fine white carbide

particles were precipitated along the boundaries as marked with short arrow in Fig. 5.2(a). Moreover, the secondary γ′ phase about 0.1~0.2 μm in size was dispersedly distributed in the grain as marked with the long arrow in Fig. 5.2(a). With the temperature increased to 550 °C, the microstructure of the alloy was similar to the former, and the fine carbide particles about 0.1~0.25 μm in size were distributed along the boundaries as marked with the short arrow in Fig. 5.2 (b). Besides, the fine γ′ precipitates were dispersedly distributed in the alloy as marked with the long arrow in Fig. 5.2(b).

The microstructure of the full heat treated alloys aged for 1000 h at 450 °C and 550 °C was shown in Fig. 5.3(a) and (b), respectively. Fig. 5.3(a) showed that the microstructure was similar to the one of the aged-free alloy, and the grain size was about 15~20 μm. Moreover, a few coarse γ′ phase was precipitated along the grain boundaries, and the size of γ′ precipitates was about 1~2 μm as shown in Fig. 5.3(a). As the aging temperature increased to 550 °C and kept for 1000 h, no obvious distinction on the size of the grain and coarse γ′ phase was detected, as shown in Fig. 5.3(b).

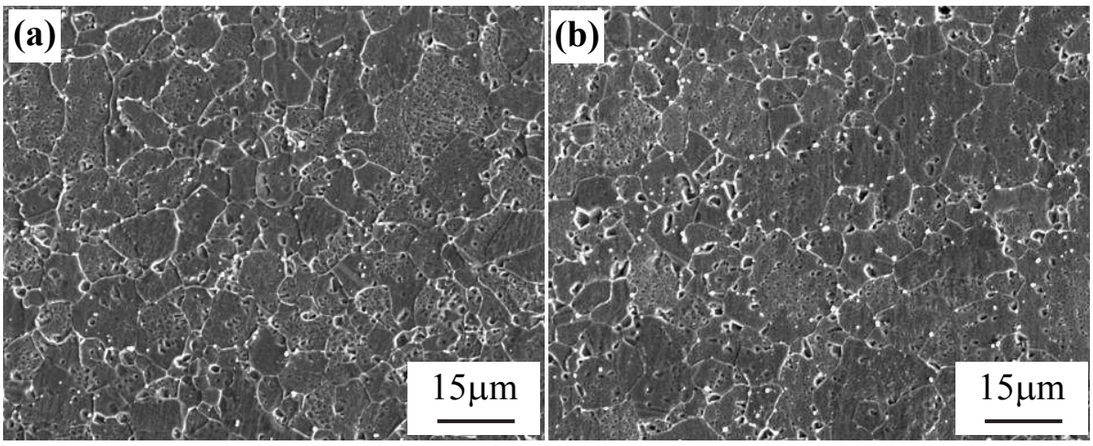

Fig. 5.3. Microstructure of the alloy aged for 1000 h at different temperatures. (a) 450 °C, (b) 550 °C

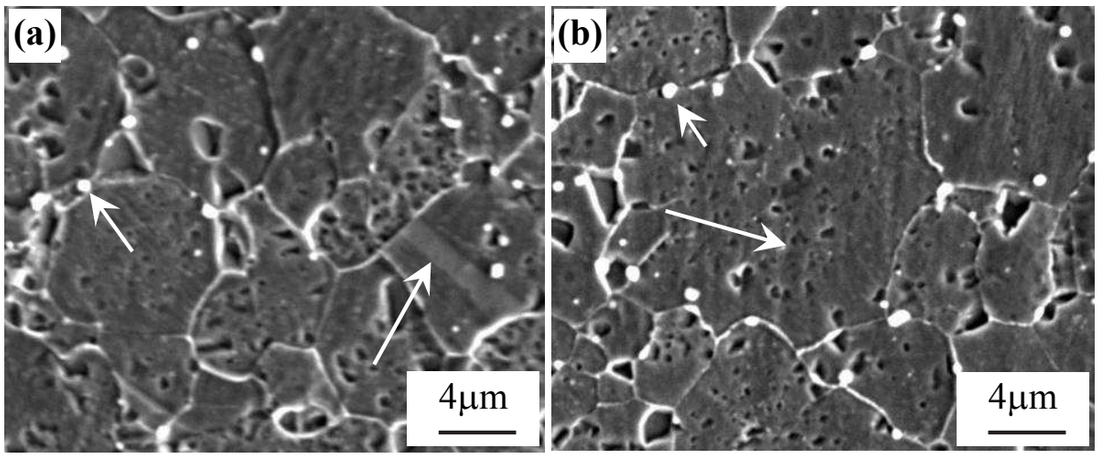

Fig. 5.4. Magnified morphology of the alloy aged for 1000 h at different temperatures. (a) 450 °C, (b) 550 °C

After aged for 1000 h at 450 °C and 550 °C, the magnified morphology of the alloy was shown in Fig. 5.4. Figure 5.4(a) shown that, after aged for 1000 h at 450 °C, some fine white carbide particles were precipitated along the boundaries as marked by the short arrow in Fig. 5.4 (a). Besides, twinning appeared obviously in the alloy as marked with the long arrow in Fig. 5.4(a). With the aging temperature increased to 550 °C, the microstructure of the alloy was similar to the former, and some fine white carbides distributed along the boundaries as marked with the short arrow in Fig. 5.4(b). Moreover, the secondary γ′ phase about 0.1~0.2 μm in size was dispersedly precipitated in the grain as marked with the long arrow in Fig. 5.4(b).

5.2 Influence of aging time on misfits

After FGH95 alloy was full heat treated, the microstructure of the alloy consisted of γ-matrix, γ′ phase and carbide particles. Thereinto, the ordered γ′ phase was coherently embedded in the γ matrix. Besides, both γ and γ′ phases have the FCC structure and close lattice parameters. Moreover, the coherent interfaces was kept in between the γ′/γ phases, and the certain misfits occurred in the interfaces of γ′/γ phases. The equations of calculating the parameters and misfit may be expressed as follow:

$$2d\sin\theta = \lambda \tag{5.1}$$

$$a = d\sqrt{\mathrm{h}^2 + \mathrm{k}^2 + \mathrm{l}^2} \tag{5.2}$$

$$\delta(\%) = \frac{2(a_{\gamma'} - a_{\gamma})}{(a_{\gamma'} + a_{\gamma})} \times 100\% \tag{5.3}$$

Where, d is crystal plane distance, θ is diffraction angle, λ = 0.154 nm, α is lattice parameter, (h, k, l) is crystal plane indexes and δ is the lattice misfit.

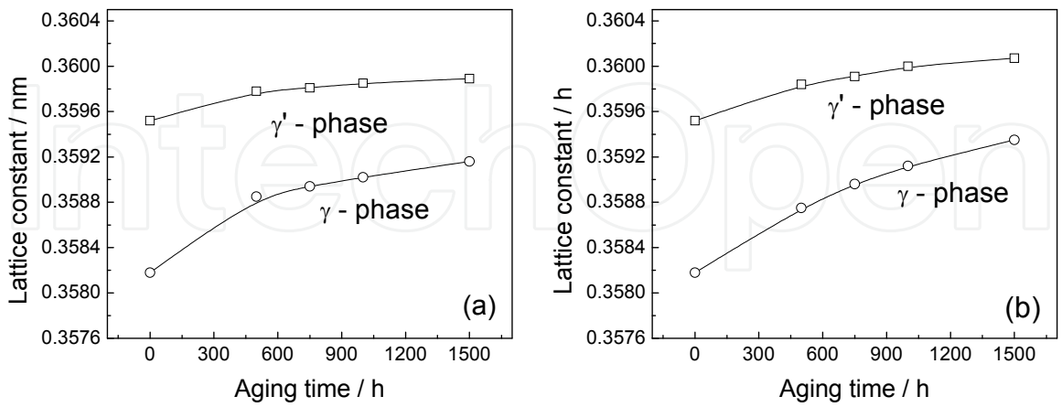

Fig. 5.5. Dependence of aging time and lattice parameters of γ/γ′ phases at different temperatures. (a) 450 °C, (b) 550 °C

After the fully heat treated alloys aged for 500 h, 750 h, 1000 h and 1500 h at 450 °C and 550 °C, the XRD curves of the alloys were measured, in which the located angles were

chosen to separate the diffraction peaks of γ and γ′ phases for measuring the crystal plane distance of γ and γ′ phase in the alloy. In the further, the lattice parameters and misfits of the alloys were calculated according to the equations (5.2) and (5.3), and the dependence of the lattice parameters and aged time at different temperatures was shown in Fig. 5.5. Figure 5.5(a) shown that the parameters of γ and γ′ phases increased gradually with the aging time at 450 °C, and the parameter increment of γ phase was more than the one of γ′ phase. With the aging temperature increased to 550 °C, the trend of the parameter increment was similar to the former, but the parameter increment of γ and γ′ phases was larger than the former, as shown in Fig. 5.5(b).

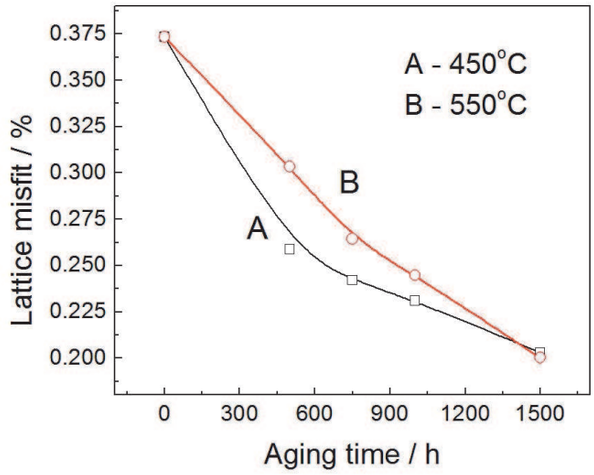

Fig. 5.6. Relationship between the lattice misfit and aging time at different temperatures

The relationship between the lattice misfit and aging time at different temperatures was shown in Fig. 5.6. This indicated that the lattice misfits decreased from 0.3734% to 0.2030% as the aging time prolonging at 450 °C as marked with letter A in Fig. 3.6. With the aging temperature increased to 550 °C, the lattice misfit decreased from 0.3734% to 0.2002% as marked with letter B in Fig. 3.6. Thereinto, the bigger difference between the lattice misfits of the alloys aged at 450 °C and 550 °C appeared in the periods of aging for 500 h and 1000 h.

6. Creep behaviors and relative parameters

6.1 Effect factors of solution temperature on creep properties

6.1.1 Influence of solution temperature on creep properties

After the 1120 °C HIP alloy solution treated at 1160 °C and cooled in molten salt at 583 °C and twice aging treated, creep curves of the alloy under different conditions are shown in Fig. 6.1. Figure 6.1(a) was the creep curves measured under different applied stresses at 650 °C. Under the applied stress of 1020 MPa, the alloy displays the shorter initial creep stage and longer steady creep stage, besides, the alloy displays the lower strain rate and longer creep lifetime about 156 h. With the applied stress enhanced to 1034 MPa, the strain rate of the alloy during steady state creep increased, and the lifetime of the alloy decreased to 104 h. As the applied stress enhanced to 1050 MPa, the creep lifetime of the alloy decreased sharply to 51 h. This indicates that, in the ranges of the applied stresses, the alloy is not sensitive to the applied stress at 650 °C.

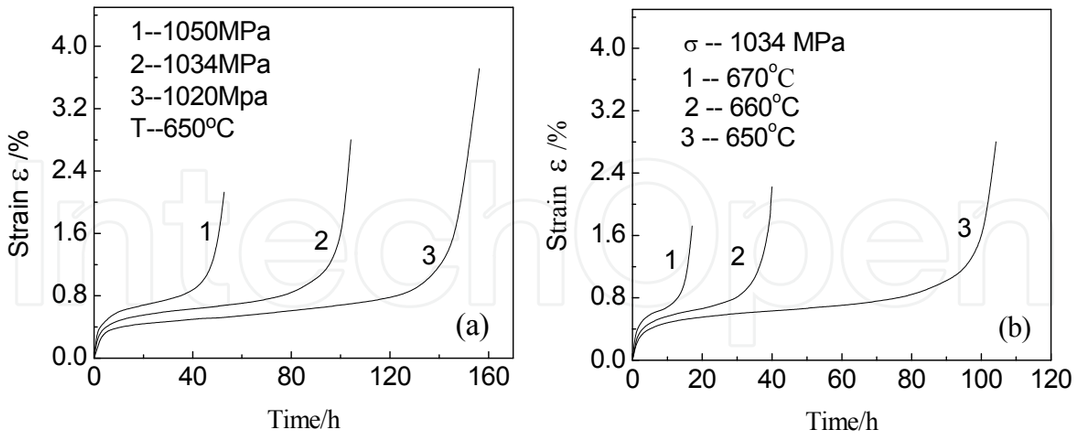

Fig. 6.1. After fully heat treated, creep curves of 1120 °C HIP alloy at different conditions (a) Applied various stresses at 650 °C, (b) 1034 MPa at various temperatures

The creep curves of the alloy under the conditions of 1034 MPa and different temperatures are shown in Fig. 6.1(b), illustrating that the alloy possesses the lower strain rate and longer creep lifetime under the applied stress of 1034 MPa at 650 °C, and the strain rate of the alloy during steady state creep was measured to be about 0.00367%/h, the creep lifetime of the alloy was about 104 h. With the creep temperature increased to 660 °C, the strain rate of the alloy during steady state creep increased to 0.00825%/h, and the creep lifetime decreased sharply to 40 h. As the temperature increased to 670 °C, the strain rate during steady state creep further enhanced to 0.01792%/h, and the lifetime of the alloy decreased to 17 h. This indicates that the alloy has an obvious sensitive to the applied temperature.

Under the applied stress of 1034 MPa at 650 °C, creep curves of the alloy solution treated at different temperatures were shown in Fig. 6.2. The creep curve of the alloy solution treated at 1150 °C was marked by letter A in Fig. 6.2, through which the strain rate of the alloy during steady state creep was measured to be 0.0102%/h, the lasting time was about 40 h, and the creep lifetime of the alloy was measured to be 67 h. The creep curve of the alloy solution treated at 1160 °C was marked by letter B in Fig. 6.2, indicating that the alloy displays a lower strain rate during steady-state creep, and the creep lifetime of the alloy was measured to be 104 h. When the solution temperature increased to 1165 °C, the creep lifetime of the alloy was measured to be about 9 h, as marked by letter C in Fig. 6.2.

After solution treated at different temperatures, the creep lifetimes of the alloy under the applied various stresses and temperatures are measured as listed in Table 6.1. It may be understood from Table 6.1 that, under the applied stress of 1034 MPa at 650 °C, the lifetime of the alloy solution treated at 1150 °C was measured to be 67 h. As the solution temperature enhanced to 1160 °C, the lifetime of the alloy increased to 104 h. When the solution temperature enhanced further to 1165 °C, the lifetime of the alloy decreased rapidly to 9 h, as shown in Table 6.1. This indicates that the solution temperature has an obvious influence on the creep lifetimes of the alloy.

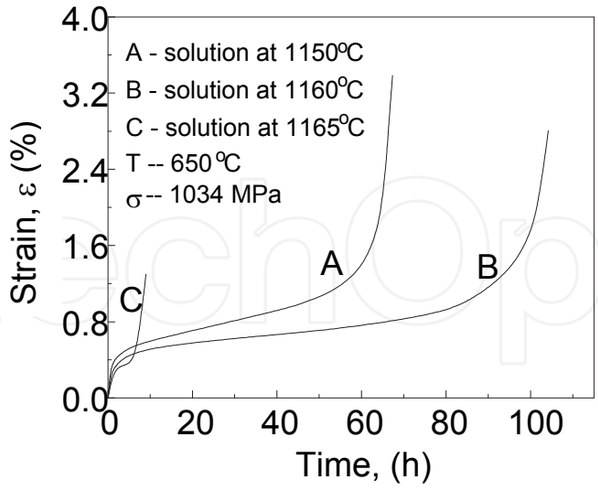

Fig. 6.2. Under the applied stress of 1034 MPa at 650 °C, creep curves of the alloy solution treated at different temperatures

After solution treated at 1150 °C, the lifetime of the alloy under the applied stress of 1020 MPa at 650 °C was about 95 h, and the strain rate during steady state creep was measured to be about 0.00827%/h. The lifetime of the alloy decreased to 67 h as the applied stress increased to 1034 MPa at 650 °C, and the creep lifetime of the alloy decreased to 37 h as the applied stress increased to 1050 MPa at 650 °C. And the alloy solution treated at 1160 °C displays also the similar regularity under the experimental conditions. This indicates that the alloy has an obvious sensitive to the applied stresses and temperatures.

Solution Temp. (°C)	650 °C									1034 MPa					
	1020 MPa			1034 MPa			1050 MPa			660 °C			670 °C		
	t_f (h)	δ (%)	$\dot{\varepsilon}$ (%/h)	t_f (h)	δ (%)	$\dot{\varepsilon}$ (%/h)	t_f (h)	δ (%)	$\dot{\varepsilon}$ (%/h)	t_f (h)	δ (%)	$\dot{\varepsilon}$ (%/h)	t_f (h)	δ (%)	$\dot{\varepsilon}$ (%/h)
1150	95	4.2	0.00827	67	3.4	0.0102	37	3.2	0.0129	26	3.6	0.0208	12	2.3	0.0418
1160	156	3.7	0.00307	104	2.8	0.00367	51	2.1	0.00456	40	2.2	0.00825	17	1.7	0.0179
1165	–	–	–	9	1.3	0.00304	–	–	–	–	–	–	–	–	–

Table 6.1. Effect of solution temperature on stress rupture properties of FGH95 alloy

6.1.2 Influence of quenching methods on creep properties

After the alloy was solution treated at 1150 °C and cooled in oil bath at 120 °C, the creep curves of the alloy at different conditions were measured as shown in Fig. 6.3. Under the applied stress of 1034 MPa at different temperatures, the creep curves of the alloy were shown in Fig. 6.3(a), it indicated that the alloy possessed the lower strain rate and longer creep lifetime of about 380 h at 630 °C.

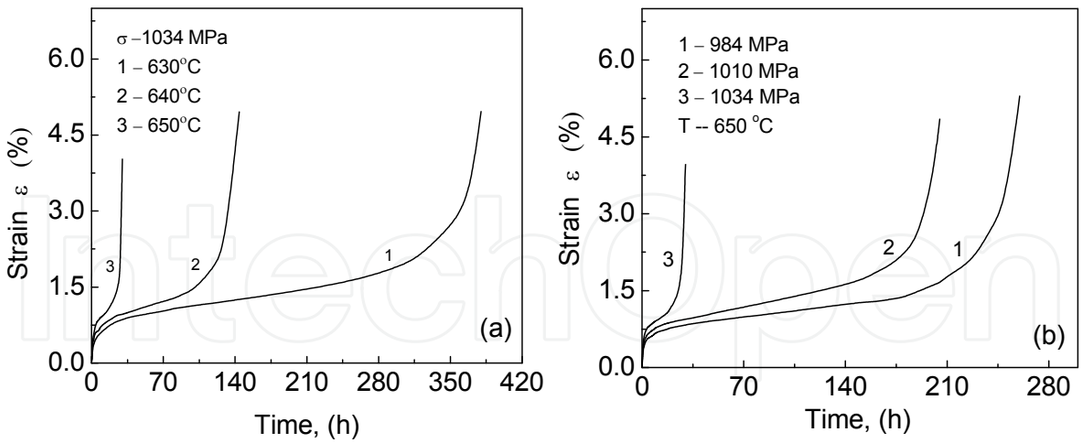

Fig. 6.3. Creep curves of the alloy cooled in oil bath at different conditions. (a) Creep curves of the alloy under the applied stress of 1034 MPa at various temperatures, (b) creep curves of the alloy under the applied different stresses at 650 °C

As the creep temperature increased to 640 °C, the lifetime of the alloy decreased to 144 h. When the creep temperature increased to 650 °C, the lifetime of the alloy decreased rapidly to 32 h. This indicates that the alloy had an obvious sensitive to the applied temperatures. While the creep curves of the alloy under the applied different stresses at 650 °C were measured as shown in Fig. 6.3(b). Under the applied stress of 984 MPa, the alloy displayed a shorter initial creep stage and a longer steady state stage of creep, and the creep lifetime of the alloy was measured to be about 260 h. The lifetime of the alloy decreased to 205 h as the applied stress enhanced to 1010 MPa, but the creep lifetime of the alloy at 650°C/1034 MPa deceased rapidly to 32 h. This indicates that the alloy possessed an obvious sensitive to the applied stress when the applied stress was over 1010 MPa.

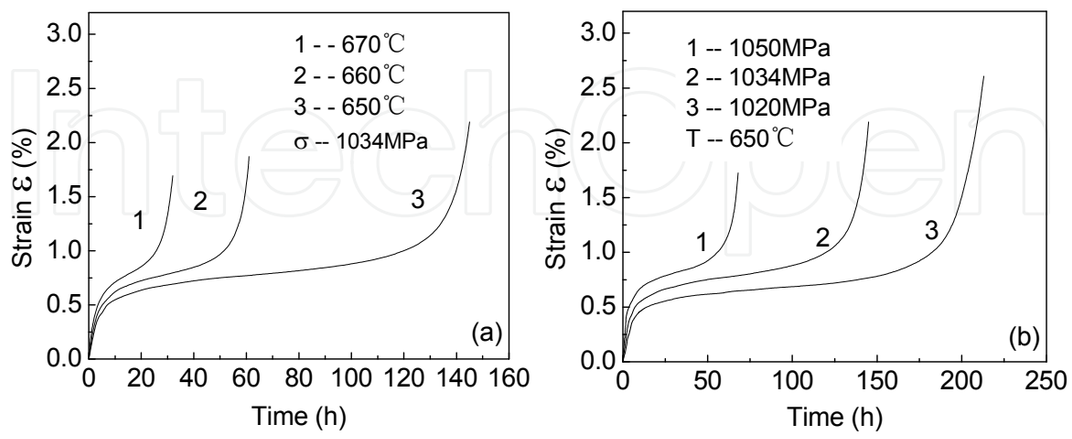

Fig. 6.4. Creep curves of the alloy cooled in molten salt at 583 °C at different conditions. (a) Creep curves of alloy under applied stress of 1034 MPa at various temperatures, (b) creep curves of alloy under the applied different stresses at 650 °C

After the solution treated at 1160 °C and cooled in molten salt at 583 °C, the creep curves of the alloy at different conditions were shown in Fig. 6.4. Under the applied stress of 1034 MPa at different temperatures, the creep curves of the alloy were measured as shown in the Fig. 6.4(a), indicating that the alloy displayed a lower strain rate and creep lifetime of about 145 h at 650 °C. As the temperature enhanced to 660 °C and 670 °C, the strain rates of the alloy during the steady state creep increased, and the creep lifetimes decreased to 60 h and 32 h, respectively. This indicates that the alloy has an obvious sensitive to the applied temperatures.

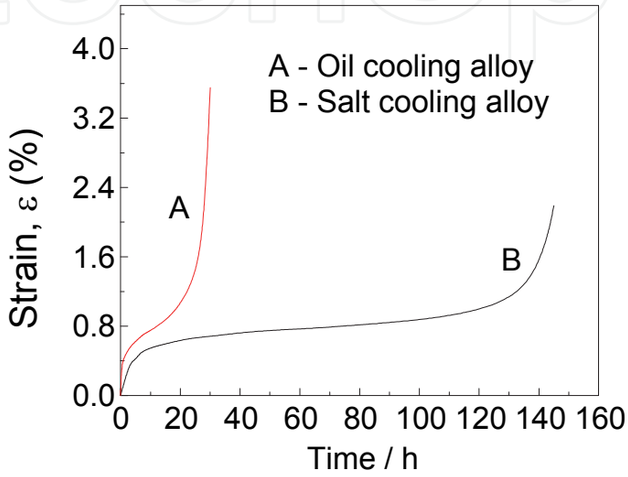

Fig. 6.5. Under the applied stress of 1034 MPa at 650 °C, creep curves of the alloy treated by different regimes

The creep curves of the alloy under the applied different stresses at 650 °C were shown in Fig. 6.4(b). The creep feature of the alloy under the applied stress of 1020 MPa displayed a shorter initial stage and longer steady state stage, and the creep lifetime of the alloy was measured to be 213 h. As the applied stress enhanced to 1034 MPa and 1050 MPa, the creep lifetimes of the alloy were measured to be 145 h and 68 h, respectively. This displays only a smaller decreasing extent of the creep lifetimes, therefore, it may be concluded that no obvious sensitivity is displayed in the alloy in the ranges of the applied stresses.

Cooling medium	Solution Temp. (°C)	Creep lifetime, t_f (h)	Elongation (%)
Oil bath	1150	32	3.9
	1160	121	2.6
Molten salt	1150	67	3.0
	1160	145	2.5

Table 6.2. Creep properties of FGH95 alloy treated by different regimes at 1034 MPa /650 °C

Under the applied stress of 1034 MPa at 650 °C, the creep curves of the alloy cooled in different mediums were shown in Fig. 6.5, indicating that, compared to the oil cooled alloy,

the alloy cooled in molten salt displayed a lower stain rate and longer creep lifetime. Moreover, the creep properties of the alloy treated by different regimes under different conditions are measured as listed in Table. 6.2, this indicates that the alloy solution treated at high temperature possesses the better creep properties.

6.2 Creep equation and relative parameters

Transient strain of the alloy occurs when the loading is applied at high temperature, and the strain rate of the alloy decreases as the creep goes on. The strain rate keeps constant once the creep enters the steady state stage, therefore, the strain rate of the alloy during steady state creep may be expressed by Dorn's law as follows:

$$\dot{\varepsilon}_{ss} = A\sigma_A^n \exp(-\frac{Q_a}{RT}) \tag{6.1}$$

where $\dot{\varepsilon}_{ss}$ is the strain rate during steady state creep, A is a constant related to the microstructure, σ_A is the applied stress, n is the apparent stress exponent, R is the gas constant, T is the absolute temperature, and Q_a is the apparent creep activation energy.

6.2.1 Influence of solution temperatures on creep relative parameters

After the 1120 °C HIP alloy solution treated at various temperatures, the creep curves of the alloy were measured in the ranges of 650 °C ~ 670 °C and 1020 MPa ~ 1050 MPa. The dependence of the strain rates of the alloy during steady-state creep on the applied temperatures and stresses was shown in Fig. 6.6. Figure 6.6(a) showed the relationship between the strain rates and the temperatures under the applied stress of 1034 MPa, and the dependence of the strain rates on the applied stresses at 650 °C was shown in Fig. 6.6(b). According to the data during the steady state creep, the creep activation energies and stress exponents of the alloys, which were solution treated at 1150 °C and 1160 °C, were calculated to be Q_A= 510.1 ± 20 kJ/mol, Q_B = 580.3 ± 20 kJ/mol and n_A=15.4, n_B=14.1, respectively.

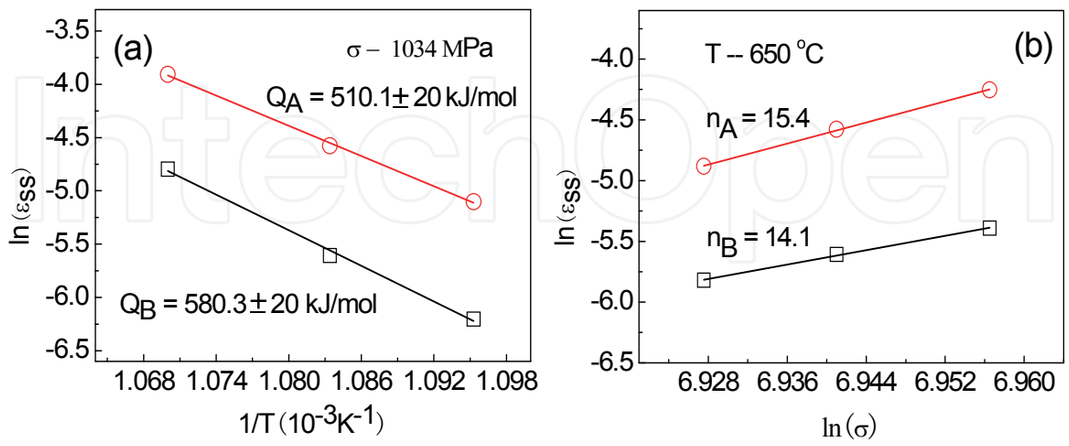

Fig. 6.6. Dependence of the strain rates during steady state creep on the applied temperatures and stresses for the alloy solution treated by different temperatures. (a) Strain rate vs. temperatures at 1034 MPa, (b) strain rate vs. the applied stress at 650 °C

6.2.2 Influence of quenching methods on creep relative parameters

After the 1180 °C HIP alloy was solution treated and cooled in different mediums, the dependences of the strain rates during steady state creep on the applied temperatures and stresses in the ranges of 650 °C ~ 670 °C and 1020 MPa ~ 1050 MPa are shown in Fig. 6.7. The relationship between the strain rates and the temperatures under applied stress of 1034 MPa was shown in Fig. 6.7(a), according to the data, the creep activation energies of the alloy treated by different regimes were calculated to be Q_A= 381.1 ± 20 kJ/mol and Q_B = 590.3 ± 20 kJ/mol, respectively. The dependence of the strain rates on the applied stresses at 650 °C was shown in Fig. 6.7(b), according to the data, the stress exponents of the alloy treated by different regimes were calculated to be n_A = 17.9 and n_B = 13.8, respectively. The values of the creep activation energies and stress exponents were measured as listed in Table 6.3. It may be concluded according to the data in Table 6.3 that the alloy cooled in molten salt displayed a better creep resistance.

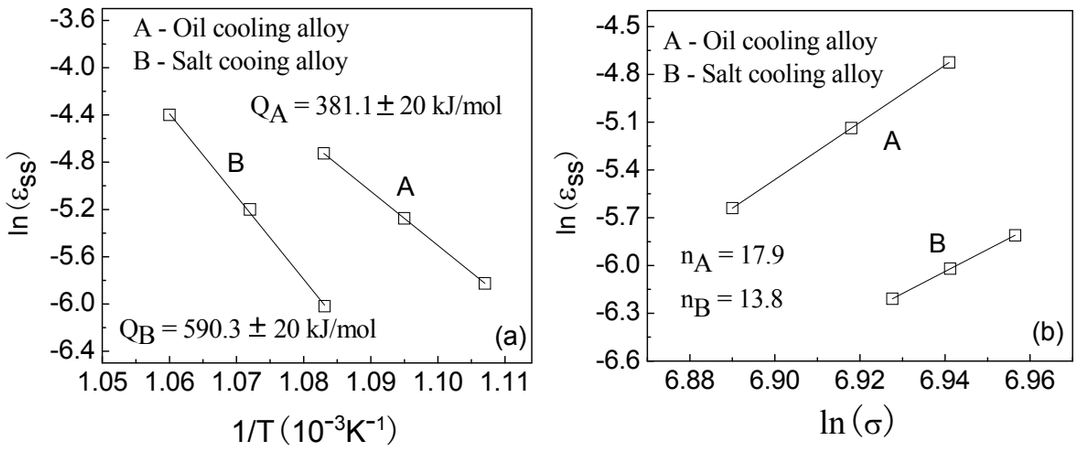

Fig. 6.7. Relationship between the strain rates and the applied temperatures, stresses for the alloy treated by different regimes. (a) Strain rates & temperatures, (b) strain rates & the applied stresses

Cooling medium	Activation energies (kJ/mol)	Stress exponents (n)
Oil bath	381.1 ± 20	17.9
Molten salt	590.3 ± 20	13.8

Table 6.3. Activation energies and stress exponents during the steady-state creep of the alloy treated by different regimes

7. Deformation mechanisms of the alloy during creep

7.1 Deformation features of alloy during creep

After the 1120 °C HIP alloy solution was treated at 1160 °C, the morphology of the alloy crept for 104 h up to rupture under the applied stress of 1034 MPa at 650 °C was shown in Fig. 7.1. Figure 7.1(a) displayed the feature of the stacking fault as marked by white arrow, and two (1/3)<112> super-Shockleys partials were located on the two sides of the stacking fault. Some dislocation loops with various sizes appeared clearly in the γ matrix of the alloy,

the smaller dislocation loop was marked with black arrow in Fig. 7.1(a), and larger dislocation loop was located in the region above the stacking fault. It could be deduced by analysis that the <110> super-dislocation shearing into the γ or γ′-phase may be decomposed to form the configuration of (1/6)<112> shockleys dislocations or (1/3)<112> super-Shockleys partials plus the stacking fault.

Some blocky carbide particles were precipitated in the local area of the alloy as marked by black arrow in Fig. 7.1(b). The grain boundary in the alloy was marked by white arrow in Fig. 7.1(c), and dislocations tangles were piled up in the region B near the boundary, which suggested that the boundaries may effectively hinder the dislocation movement during creep. Besides, the morphology of <110> super-dislocation shearing into the γ′-phase was marked by the black arrow, and the stacking fault formed from the dislocation decomposition was marked by the letter A in Fig. 7.1(c). The blocky carbides were precipitated along the boundary as marked by the black arrow in Fig. 7.1(d), and some dislocations were piled up in the regions near the carbides, which indicated that the carbide particles can effectively hinder the dislocation movement. But, the facts that significant amount of dislocations were piled up in the regions near the boundaries can cause the stress concentration to promote the initiation and propagation of the micro-crack along the boundaries as the creep goes on.

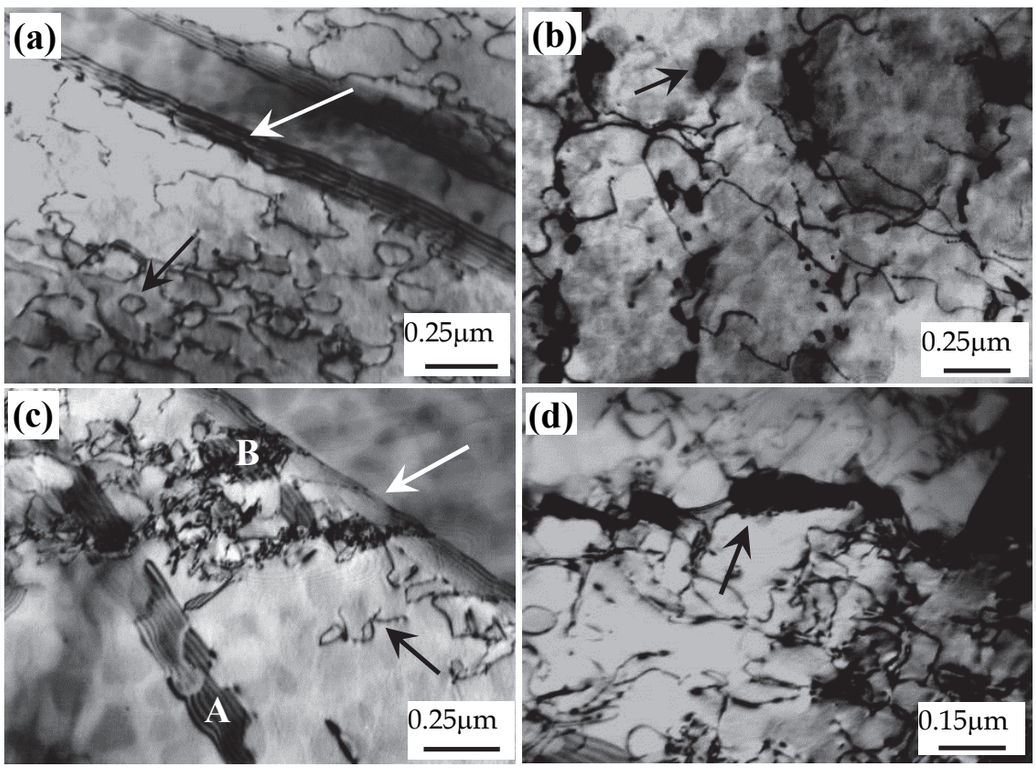

Fig. 7.1. Microstructure of the alloy after (solution treated at 1160 °C) crept for 104 h up to fracture at 650 °C/1034 MPa. (a) dislocation loops in the alloy, (b) carbide particles precipitated within the grain, (c) morphology of the super-dislocation shearing into γ′ phase as marked by black arrow, the stacking fault in the region A and dislocation tangles piled up in the B region near the boundary, (d) carbide particles precipitated along the boundary, and dislocation tangles piled up in the regions near the boundaries

After the 1180 °C HIP alloy solution treated at 1150 °C and cooled in the oil bath, the microstructures of the alloy crept for 260 h up to fracture under the applied stress of 984 MPa at 650 °C was shown in Fig. 7.2. The fine sphere-like γ′ particles about 0.1~0.2 μm in size were dispersedly distributed in the alloy as shown in Fig. 7.2(a), which may hinder the dislocation movement for improving the creep resistance of the alloy. During creep, the double orientation slipping of dislocations were activated in the local regions of γ matrix as shown in Fig. 7.2(b), the deformed dislocations in the form of the tangles were arranged along the level direction, the bundle-like dislocations were arranged along the upright-like direction as marked by arrows, respectively, in Fig. 7.2(b). During creep, the slipping dislocations moving to the boundary were stopped as marked by white arrow in Fig. 7.2(c), indicating that the boundary had an obvious effect on hindering the dislocations movement. Therefore, it may be concluded that the deformation feature of the alloy during creep is the double orientations slipping of dislocations activated in the γ matrix phase.

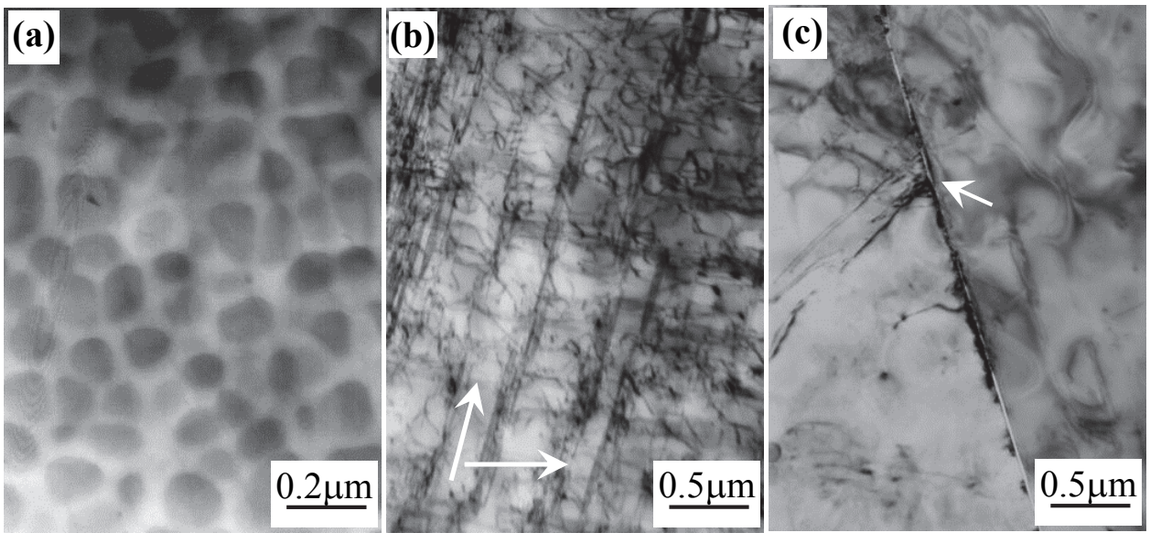

Fig. 7.2. After solution treated at 1150 °C and cooled in oil bath, microstructure of the alloy crept for 260 h up to fracture under the applied stress of 980 MPa at 650 °C. (a) Fine γ′ phase precipitated dispersedly within the grains, (b) double orientations slipping of dislocation as marked by arrows, (c) dislocations slipping stopped on the boundary

After the 1180 °C HIP alloy was solution treated at 1160 °C and cooled in the molten salt, the microstructures of the alloy crept for 72 h up to fracture under the applied stress of 1034 MPa at 650 °C was shown in Fig. 7.3. The carbide particles were precipitated along the boundaries as marked by arrow in Fig. 7.3(a), which resulted in the boundary with the uneven feature. The dislocation-free region appeared in the left side of the boundary, significant amount of dislocations were congregated in the another side of the boundaries, and the carbide particle was precipitated along the boundary as marked by the arrow in Fig. 7.3(b). It may be analyzed according to Fig. 7.3(b) that the boundaries and the carbides precipitated along the boundaries may hinder the dislocations movement for improving the creep resistance of the alloy, so that significant amount of dislocations are piled up in the right-side region of the boundary as shown in Fig. 7.3(b).

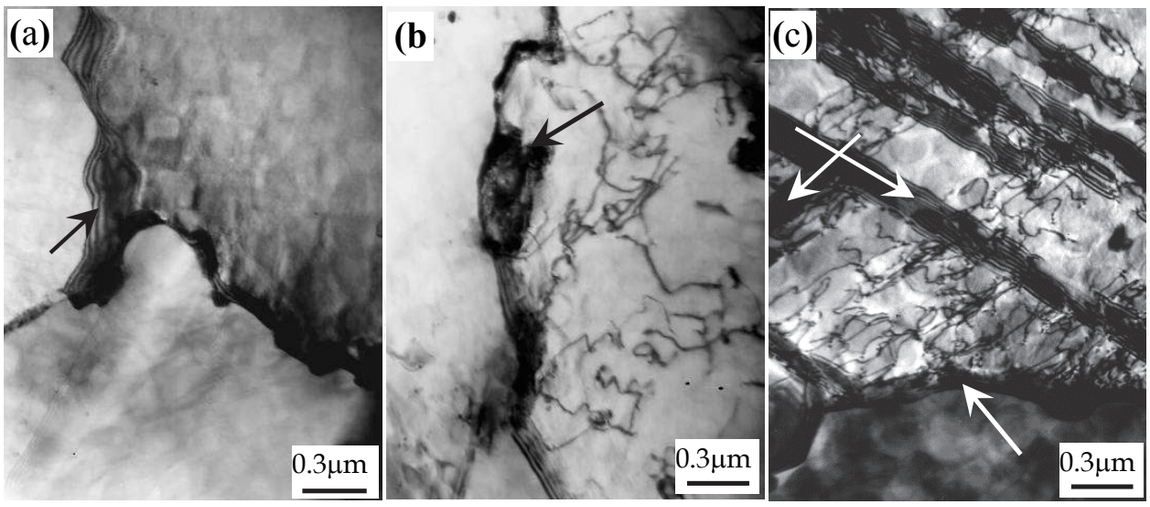

Fig. 7.3. After solution treated at 1160 °C and cooled in molten salt, microstructure of the alloy crept up to fracture at 1034 MPa / 650 °C. (a) Carbide particles precipitated along the boundary, (b) dislocation tangles piled up in the regions near the boundaries, (c) stacking fault and dislocations appeared within the grain

In the local region of the alloy, the double orientation slipping of dislocations were activated within the grain, the boundary was marked by arrow in the bottom of Fig. 7.3(c), the directions of the double orientation slipping of dislocations were marked with arrows in Fig. 7.3(c). The arrow which points to left side corresponds to the orientation of the dislocations tangle, the arrow which points to right-side corresponds to the direction of the stacking fault stripes. It may be deduced by analysis that the stacking fault is formed in between two (1/3)<112> super-Shockleys partials which originates from the decomposition of <110> super-dislocation. The configuration of the partial dislocation + stacking fault can restrain the cross-slipping of the dislocations to improve the creep resistance of the alloy.

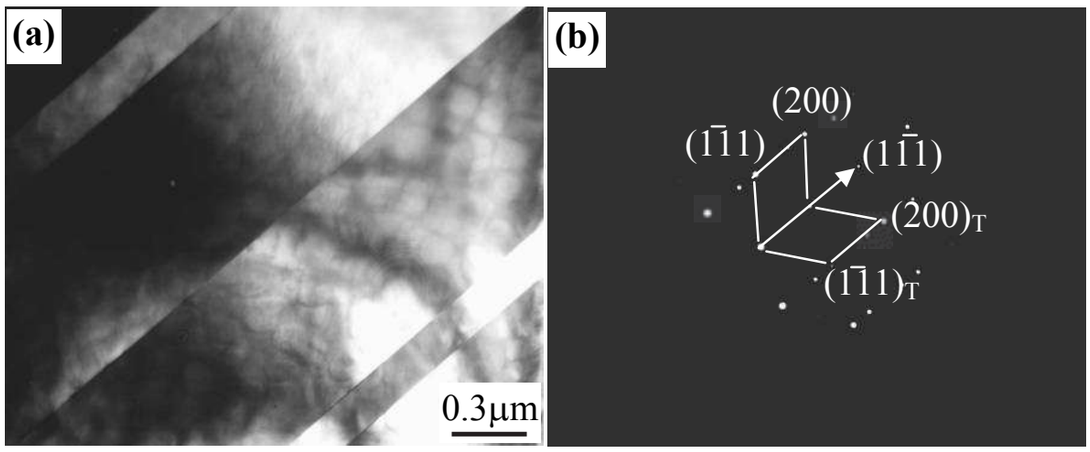

Fig. 7.4. Twinning in the alloy during creep at 650 °C/1034 MPa. (a) twinning, (b) SAD patterns

After the alloy was crept up to fracture under the applied stress of 1034 MPa at 650 °C, the feature of the twinning deformation was shown in Fig. 7.4(a), and the twinning plane was

identified as (111) plane by means of the diffraction pattern analysis as shown in Fig. 7.4(b). The blocky carbide was precipitated along the grain boundary as marked by shorter arrow in Fig. 7.5(a), and some micro-twinning was detected in the alloy as marked by black arrow. In another local area, the morphology and diffraction spots of the micro-twinning were shown in Fig. 7.5(b) and (c), this is well agreed with the result in literature (Unocic R. R. et al., 2008). The one end of the micro-twinning was stopped at the grain boundary, which suggests that the grain boundaries had an obvious effect on hindering the twinning deformation.

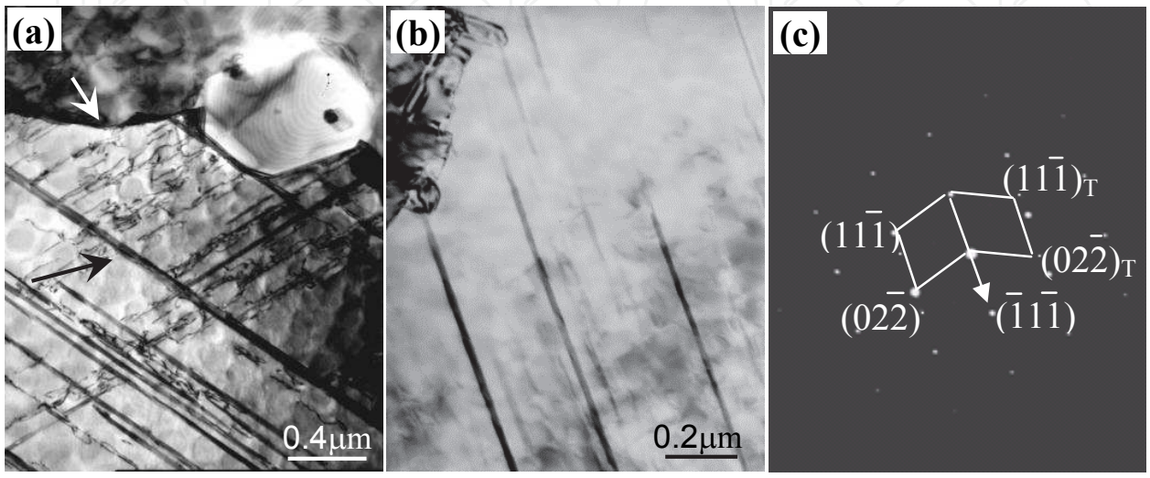

Fig. 7.5. Morphologies of the carbide precipitated along the boundary and micro-twinning formed in the alloy during creep under the applied stress of 1034 MPa at 650 °C. (a) Carbide precipitated along the boundary, (b) micro-twinning, (c) SAD patterns

7.2 Analysis on deformation features of the alloy during creep

7.2.1 Dislocation model

Significant amount of the fine γ′ particles are precipitated within the grains, which may effectively hinder the dislocation movement. When the deformed dislocations move over the γ′ phase during creep, the dislocation loops are kept around the γ′ particles as shown in Fig. 7.1(a), which suggests that the deformation feature of the alloy during creep is the dislocations moving over the γ′-phase by Orowan bypassing mechanism. It is reasonable consideration that the various spaces between the γ′ particles appear in different regions, the dislocations may bow out along the wider channels between the two γ′ particles during creep, and the bowing dislocations move over the γ′-phase by Orowan mechanism to encounter for forming the dislocation loops, as marked with black arrow in Fig. 7.1(a). When the dislocations bow out along the channels during creep, the applied stress which is enough to overcome the Orowan resistance can be expressed as follows:

$$\tau_{or} = \frac{\mu \cdot b}{L} \tag{7.1}$$

Where, μ is the shear modulus, b is the Burgers vector, and L is the space between two γ′ particles. This indicates that the resistance of the dislocation movement increases with the diminishing of the space between the γ′-particles, and the resistance of alloy enhances with the volume fraction of γ′-particles.

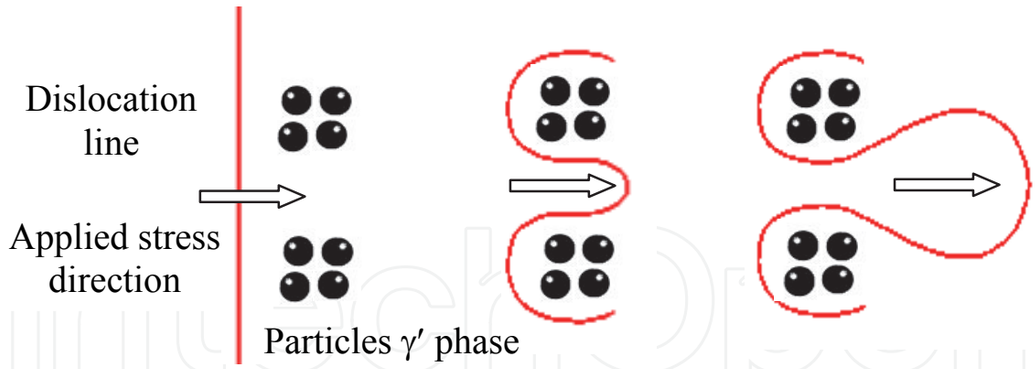

Fig. 7.6. Schematic diagram of dislocation bowing out in the congregated regions of the γ′ particles

The space between the γ′ particles diminishes when some γ′ particles are congregated together, the smaller space is measured to be L_1 = 0.03 μm as shown in Fig. 4.5(a), but the bigger space between the γ′-particles is measured to be L_2 = 0.12 μm. Compared to the bigger space, the dislocations bowing out in the regions with smaller space needs fourfold Orowan resistance according to the formula (7.1), therefore, it is difficult for the dislocations to bow out along the channels with smaller space, but they can bow out along the channels with larger space to form the larger loops as shown in Fig. 7.1(a). When the dislocations bow out along the channels with bigger space (L), the formation process of the bigger dislocation loops is schematically shown in Fig. 7.6.

In the later stage of creep, significant amount of dislocations move to the region near the γ′ particles to generate stress concentration, and when the stress value originated from the stress concentration exceeds the yield strength of γ′ phase, the <110> super-dislocation may shear into the γ′-phase, as marked by black arrow in Fig. 7.1(c). Furthermore, the <110> super-dislocations may be decomposed to form the configuration of two (1/3)<112> super-Shockleys partials and the stacking fault, as marked by letter A in Fig. 7.1(c). The critical stress of dislocation shearing into γ′ phase increases with the yield strength. And the critical stress (τ_{cs}) can be expressed as follows (Zhang J. SH., 2007) :

$$\tau_{cs} = \frac{\eta_{APB}}{b}\left(\frac{0.3 \cdot \eta_{APB} \cdot f \cdot r}{T}\right)^{1/2} \tag{7.2}$$

Where T is the dislocation line tension, r is the radius of the γ′-particle, $\boldsymbol{b}$ is the Burgers vector, f is the volume fraction of γ′ phase, and η_{APB} is the antiphase boundary energy originated from the dislocation shearing γ′ phase. It may be understood from equation (7.2) that the critical stress of dislocation shearing into γ′ phase increases with the size (r), volume fraction (f) of γ′-phase and antiphase boundary energy (η_{APB}) to improve the creep resistance of the alloy.

7.2.2 Micro-twinning model

The observed shearing process spawned the model (Unocic R. R. et al., 2008) is illustrated in Fig. 7.7. The process of shearing the larger γ′ particles is presumed to occur by the cooperative movement of the coupled (a/2)[112] dislocation (3Dα), each of which is dissociated into three (a/3)[112] partials (Dα).

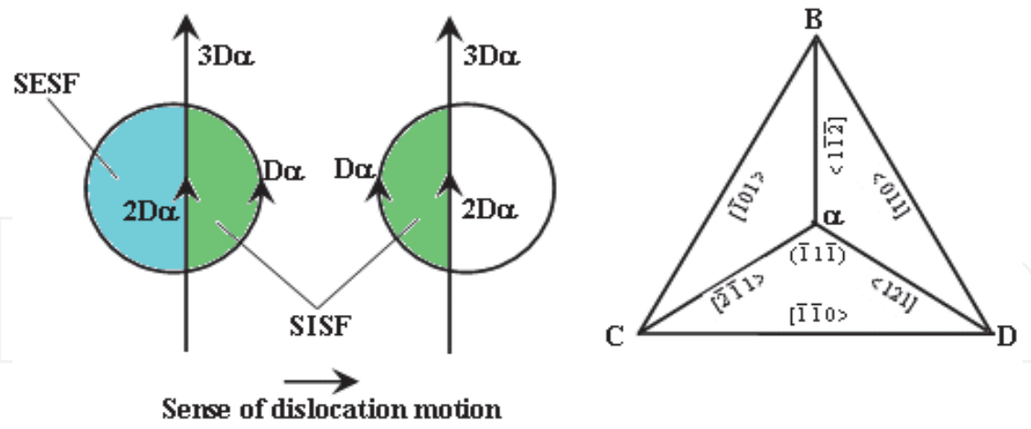

Fig. 7.7. Model of γ′ precipitate shearing by coupled Shockley partials for creating SISF/SESF pairs. After Hirth and Lothe (Unocic R. R. et al., 2008, as cited in Hirth J. P. & Lothe J., 1968)

The a<112> dislocations are hypothesized to originate from the interaction of two different a<101> super- dislocations originating from different slip systems. For example:

$$a[011] + a[101] = a[112] \tag{7.3}$$

Clearly, this model then requires a high symmetry orientation such that two slip systems experience a relatively large shear stress.

In situ deformation at higher temperature gives rise to a distinctly different mode of shearing in which the extended faults propagate continuously and viscously through both particles and matrix. These extended faults are associated with partials that move in a correlated manner as pairs. Koble (Koble M., 2001) induced that these partials may be a/6<112> partials of the same Burgers vector, and that they may be traveling in parallel {111} planes, as illustrated in Fig. 7.8. Without detailed confirmation of this hypothesis, Kolbe further deduced that these were in fact micro-twins, and that the temperature dependence of the process may be associated with recording that would ensure in the wake of twinning a/6<112> partials as they traverse the γ′ particles. The shear strain rate can be expressed as follow:

$$\dot{\gamma} = \rho_{tp} b_{tp} v = \rho_{tp} b_{tp} \frac{D_{ord} (b_{tp} / x^2)}{\ln[f_2 \Delta\Gamma / (2\tau_{eff} b_{tp} - f_2 \Gamma_{tt})} \tag{7.4}$$

Where, r_{pt} is the energy of two layered pseudo-twin, and b_{pt} is the magnitude of the Burgers vector of the twinning partials, r_{tt} is the energy of two layered true twin, ρ_{pt} is the density of mobile twinning partials, D_{ord} is the diffusion coefficient for ordering, x is the short range diffusion length (assumed to be several nearest neighbor distances, or ~2b), f_2 is the volume fraction of the secondary γ′ precipitates, f_3 is the volume fraction of the tertiary γ′ precipitates. And the effective stress (τ_{eff}) , in the presence of tertiary γ′ precipitates, is given by:

$$\tau_{eff} = \tau - \frac{f_3 \Gamma_{pt}}{2 b_{tp}} \tag{7.5}$$

The experimental values of parameters such as dislocation density ρ_{pt}, volume fraction of the secondary γ′ precipitate that are critical to the prediction can be determined directly from TEM observations. Disk alloys in this temperature regime typically exhibit the creep curves having a minimum rate, with a prolonged increase of creep rate with time. As the fine γ′ phase volume fraction decreases during thermal exposure, it is possible that the operation of 1/2[110] matrix dislocations becomes increasingly important. The coarse microstructure (small value of f_3) resulting from a slow cooling rate, the deformation is dominated by 1/2<110> dislocation activated in the matrix, and SESF shearing in the secondary γ′ precipitates.

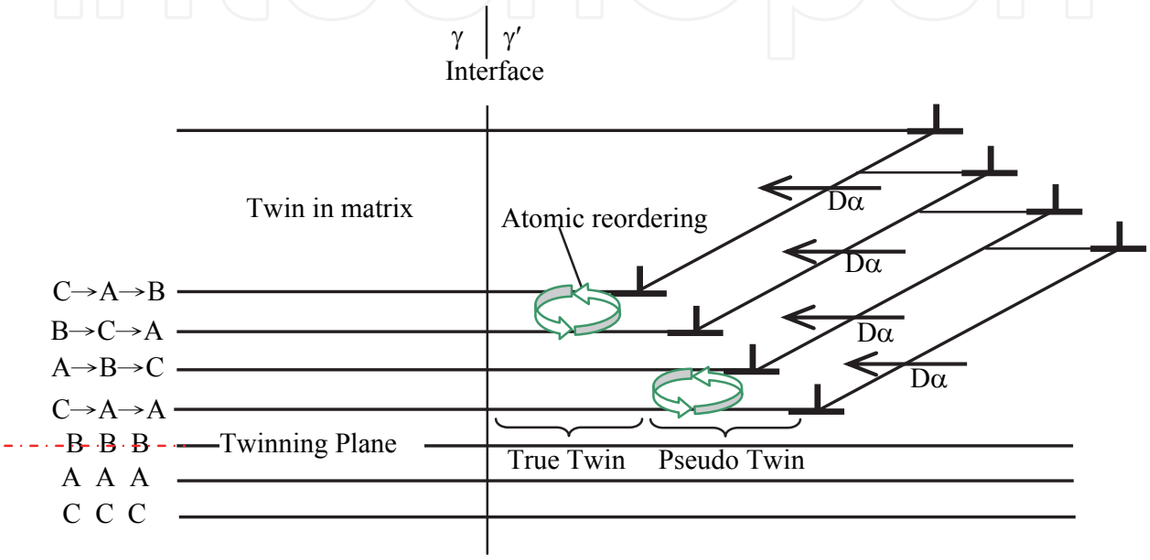

Fig. 7.8. Schematic representation of micro-twinning mechanism from shear by identical Shockley partials (Dα) transcending both the γ matrix and γ′ precipitate in adjacent {111} planes which then require atomic reordering in γ′ to convert stacks of CSF into a true twinned structure. After Kolbe (Koble M., 2001)

8. Fracture features of the alloy during creep

8.1 Influence of solution temperature on fracture feature of alloy during creep

After the 1120 °C HIP alloy was solution treated at 1150 °C and isothermal quenched in molten salt at 583 °C, the morphology of the alloy crept for different time under the applied stress of 1034 MPa at 650 °C was shown in Fig. 8.1. The applied stress direction was marked with the arrow in Fig. 8.1(a), after the alloy was crept for 40 h, some slipping traces appeared on the surface of the sample, and some parallel slipping traces were displayed within the same grain. Moreover, the various orientations of the slipping trace appeared within the different grains. Besides, the kinking of the slipping traces appeared in the region of the boundaries as marked by arrow in Fig. 8.1(a). After crept for 67 h up to rupture, the surface morphology of the alloy was shown in Fig. 8.1(b), indicating that the amount of the slipping trace increased as the creep went on, and the slipping traces were deepened to form the slipping steps on the surface of the specimen. Moreover, the bended slipping traces appeared in the boundary regions, as marked by longer arrow in Fig. 8.1(b), which was

attributed to the effect of the flow metal in the γ′-free phase zone where is lower in strength. Besides, the cracks were initiated in the distortion regions of slipping traces as marked by shorter arrow in Fig. 8.1(b).

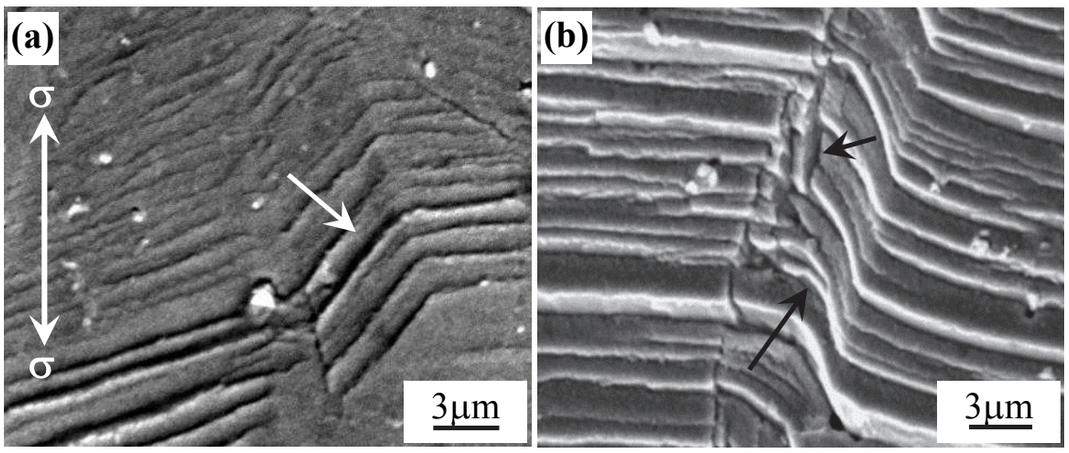

Fig. 8.1. Surface morphology of the alloy crept for different time up to fracture. (a) After crept for 40 h, a few slipping traces appeared within the different grains, (b) after crept up to fracture, significant amount of the slipping traces appeared on the sample surface, and cracks appeared in the region near the boundary as marked by arrow

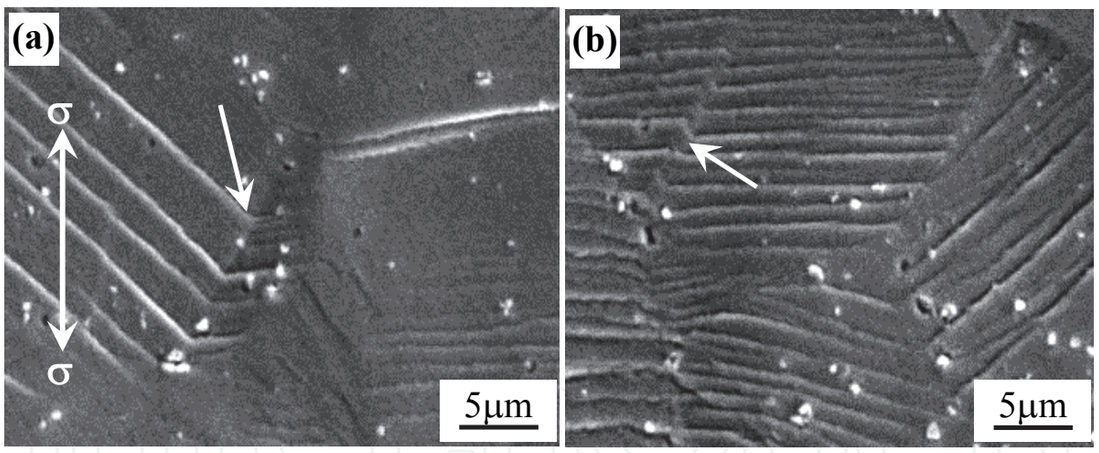

Fig. 8.2. After solution treated at 1160 °C, surface morphology of the alloy crept for different time. (a) After crept for 60 h, a few slipping traces appeared within the different grains, (b) after crept for 80 h, significant amount of the slipping traces appeared in the surface of the sample

After 1120 °C HIP alloy was solution treated at 1160 °C and twice aged, the morphology of the alloy crept for different time under the applied stress of 1034 MPa at 650 °C was shown in Fig. 8.2. The direction of the applied stress was marked by arrows, after the alloy was crept for 60 h, the morphology of the slipping traces on the sample surface was shown in Fig. 8.2(a), which displayed the feature of the single orientation slipping appearing within the different grains. And the intersected of the slipping traces appeared in the boundary region as marked by arrow in Fig. 8.2(a), which indicated that the boundary may hinder the

slipping of the traces to change their direction. When crept for 80 h, the quantities of the slipping traces on the sample surface increased obviously, as shown in Fig. 8.2(b), and some white blocky carbide particles were precipitated within the grains.

After solution treated at 1160 °C and twice aged, the surface morphology of the alloy crept up to rupture under the applied stress of 1034 MPa at 650 °C was shown in Fig. 8.3. As the creep went on, the quantities of the slipping traces increases gradually (the direction of the applied stress shown in Fig. 8.3(a), which may bring out the stress concentration to promote the initiation of the micro-cracks along the boundary which was vertical to the stress axis as marked by the letter A and B in Fig. 8.3(a). In the other located region, the morphology of the crack initiation was marked by letter C in Fig. 8.3(b), the micro-cracks displayed the non-smooth surface as marked by arrow, and the white carbide particle was located in the crack, it indicated that the carbide particles precipitated along the boundary may restrain the cracks propagating along the boundaries to enhance the creep resistance of the alloy.

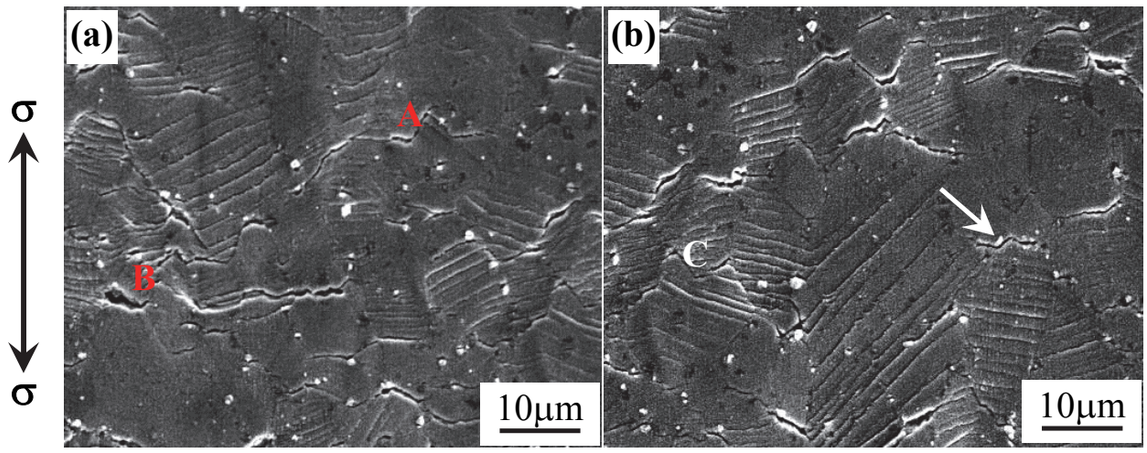

Fig. 8.3. Cracks initiated and propagated along the boundary. (a) Crack initiated along the boundaries vertical to the stress axis, (b) crack propagated along the boundaries as marked by arrow

After the alloy crept up to fracture, the morphology of the sample polished and eroded was shown in Fig. 8.4. Some carbide particles were located in the boundaries as shown in Fig. 8.4(a), which may hinder the slipping of the dislocation for enhancing the creep resistance of the alloy. Moreover, the unsmooth surface of the cracks appeared in the fracture regions as marked by white arrow in Fig. 8.4(a). However, when no carbide particles were precipitated along the boundaries, the crack after the alloy crept up to fracture displayed the smooth surface as marked with the letter D and E in Fig. 8.4(b).

It may be thought by analysis that, although the carbide particles may hinder the dislocations movement for improving the creep resistance of alloy, the carbides located in the regions near the boundaries may bring about the stress concentration to promote the initiation and propagation of the cracks along the boundary as marked with the arrow in Fig. 8.4(a). Therefore, the fracture displayed the non-smooth surface due to the pinning effect of the carbide particles precipitated along the boundaries to restrain the boundaries slipping during creep. Though the carbide particles precipitated along the boundaries can improve the cohesive strength of the boundaries, the micro-cracks are still initiated and propagated along the boundaries, which suggests that the boundaries are still the weaker regions for causing fracture of the alloy during creep.

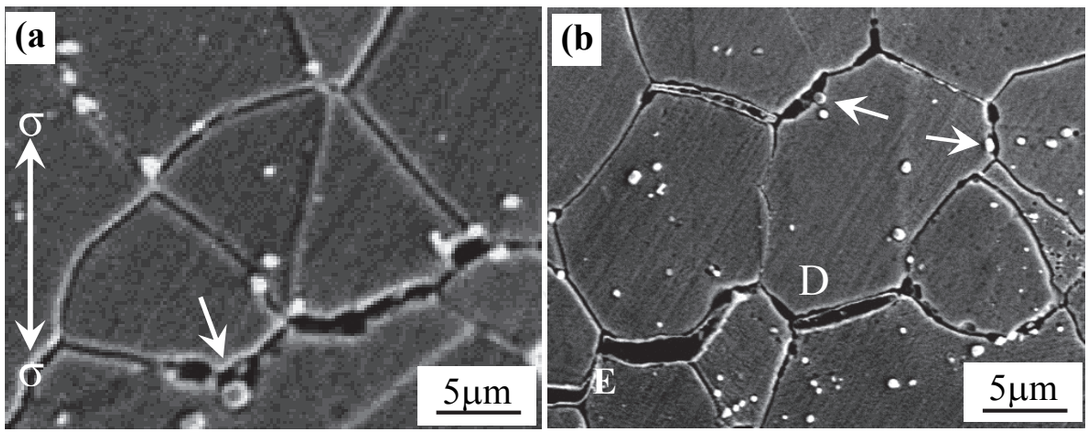

Fig. 8.4. After solution treated at 1160 °C, surface morphology of the alloy crept up to fracture. (a) Carbide particles near the crack along the boundary marked by arrow, (b) morphology of cracks propagated along the boundary marked by arrow

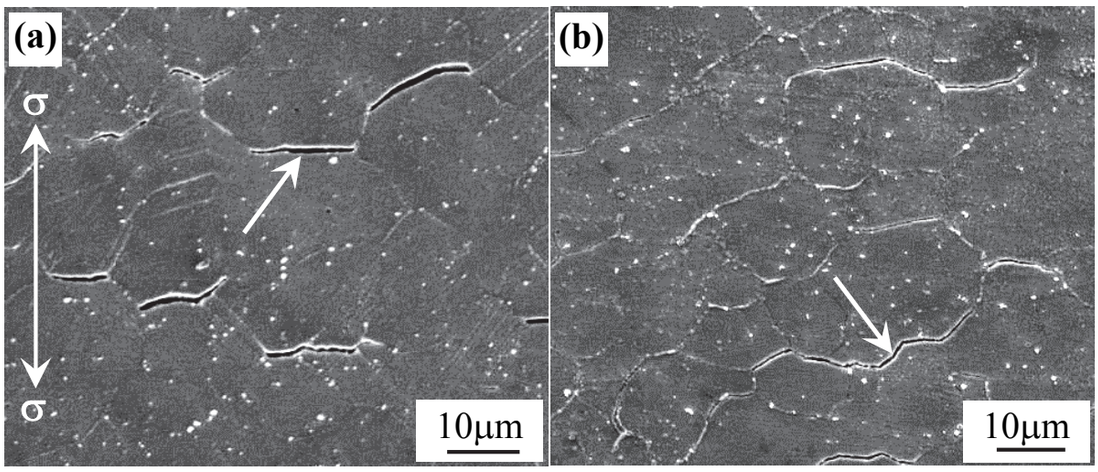

Fig. 8.5. After solution treated at 1165 °C, surface morphology of the alloy crept for 9 h up to fracture. (a) Crack initiated along the boundary as marked by arrow, (b) cracks propagated along the boundary as marked by arrow

After solution treated at 1165 °C and aged, the surface morphology of the alloy crept for 9 h up to rupture under the applied stress of 1034 MPa at 650 °C was shown in Fig. 8.5. A few slipping trace appeared only on the surface of the alloy, and some micro-cracks were initiated along the boundaries vertical to the applied stress axis, as marked by arrow in the Fig. 8.5(a). As the creep went on, the morphology of the micro-crack propagated along the boundary was shown in Fig. 8.5(b), in which the fracture of the alloy displayed the smooth surface. It may be deduced according to the feature of the smooth fracture that the carbide films precipitated along the boundaries has an important effect on decreasing the stress fracture properties of the alloy. The carbide films were formed along the boundaries during heat treated, which reduced the cohesive strength between the grains. Therefore, the micro-crack was firstly initiated along the boundaries with the carbide films, and propagated along the interface between the carbide films and grains, which resulted in the formation of the smooth surface on the fracture, and decreased to a great extent the creep properties of the alloy.

After the alloy was crept for 9 h up to rupture under the applied stress of 1034 MPa at 650 °C, the surface morphology after the sample was polished and eroded was shown in Fig. 8.6. The carbide films were continuously formed along the boundaries as marked with the long arrow in Fig. 8.6(a), the direction of the applied stress was marked by arrow, the micro-crack was initiated along the carbide film, as marked by shorter arrow in Fig. 8.6(a). As the creep went on, the morphology of the crack propagated along the boundaries was shown in Fig. 8.6(b), the fracture after the crack was propagated displayed the smooth surface, and the white carbide film was reserved between the tearing grains marked by arrow in Fig. 8.6(b), which displayed an obvious feature of the intergranular fracture of the alloy during creep. It can be thought by analysis that the carbide films precipitated along the boundaries, during heat treated, possessed the hard and brittle features and weakened the cohesive strength between the grains. Therefore, the micro-crack was firstly initiated along the carbide films and propagated along the interface between the grains and carbide films, which resulted in the formation of the smooth surface on the fracture, so the alloy had the lower toughness and shorter creep lifetime. Moreover, it was identified by means of composition analysis under SEM/EDS that the elements Nb, Ti, C and O were rich in the white particles on the surface of the samples, as shown in Fig. 8.2, Fig. 8.3 and Fig. 8.5, respectively, therefore, it is thought that the white particles on the surface of the samples are the oxides of the elements Nb, Ti and C.

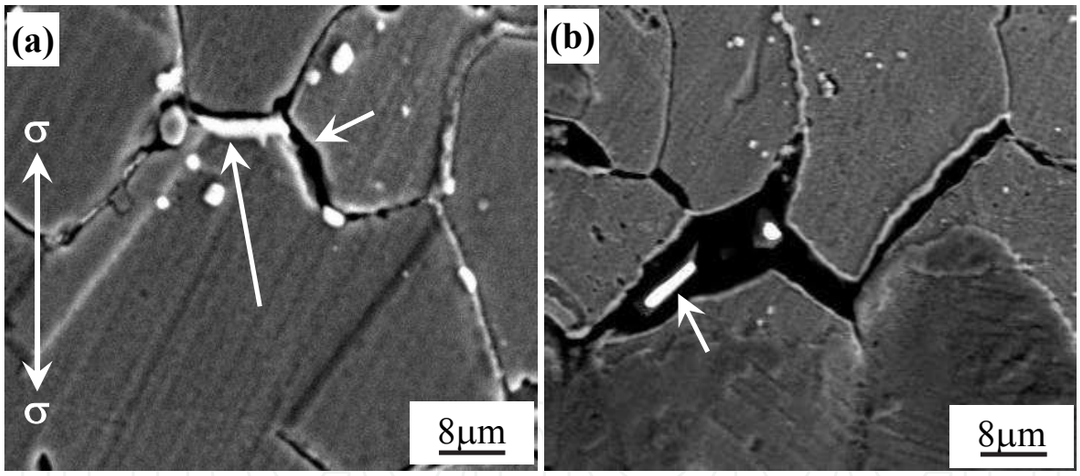

Fig. 8.6. After solution treated at 1165 °C, surface morphology of the alloy crept for 9 h up to fracture. (a) Crack initialed along the boundary marked by arrow, (b) morphology of cracks propagated along the boundary marked by arrow.

8.2 Influence of quenching temperatures on fracture feature of alloy during creep

After the 1180°C HIP alloy was solution treated at 1150 °C and cooled in oil bath at 120 °C, the morphologies of the alloy crept for 260 h up to rupture under the applied stress of 984 MPa at 650 °C were shown in Fig. 8.7. If the PPB region between the powder particles was regard as the grain boundaries as shown in Fig. 8.7(a), the grain boundaries after the alloy was crept up to rupture were still wider, and the ones were twisted into the irregular piece-like shape as marked by arrow in Fig. 8.7(a).

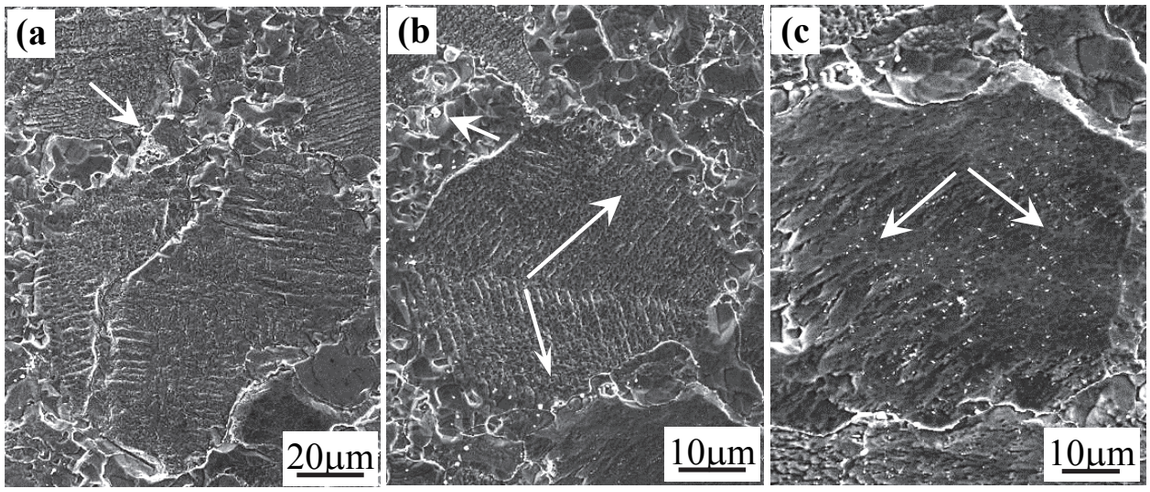

Fig. 8.7. Microstructure of alloy after crept up to fracture under the applied stress of 984 MPa at 650 °C. (a) Wider grain boundaries broken into the irregular shape as marked by arrow, (b) traces with double orientations slipping feature appeared within the grain as marked by arrows, (c) finer particles precipitated along the slipping traces

Some irregular finer grains were formed in the boundary regions, and displaying a bigger difference in the grain sizes. Some coarser γ′ precipitates were precipitated in the boundaries region in which the creep resistance is lower due to the spareness of the finer γ′ phase. The severed deformation of the alloy occurred firstly in the boundary regions during high stress creep, which resulted in the boundaries broken into the irregular piece-like shape. At the same time of the severed deformation, the traces with double orientations slipping feature appeared within the grains as marked by arrows in Fig. 8.7(b), and some particles were precipitated in the boundaries region as marked by short arrow in Fig. 8.7(b). Moreover, the finer white particles were precipitated in the regions of the double orientations slipping traces as marked by arrows in Fig. 8.7(c), and the white particles were distinguished as the carbides containing the elements Nb, Ti and C by means of SEM/EDS composition analysis.

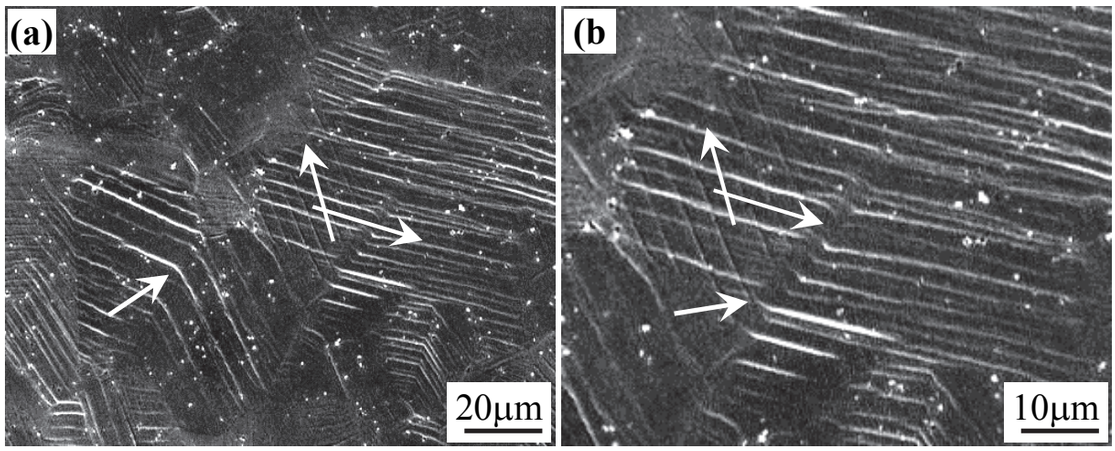

Fig. 8.8. Microstructure after the molten salt cooled alloy crept up to fracture under the applied stress of 1034 MPa at 650 °C. (a) Traces of the double orientations slipping appeared within the grains, (b) magnified morphology of the slipping traces

After solution treated at 1150 °C, and cooled in molten salt at 583 °C, the morphology of the alloy crept for 67 h up to rupture under the applied stress of 1034 MPa at 650 °C was shown in Fig. 8.8. This indicated that the traces with the double orientations slipping feature appeared within the grain, and the various orientations of the slipping traces appeared in the different grains, thereinto, the directions of the thicker and fine traces were marked by the arrows, respectively, in Fig. 8.8(a). Moreover, the traces with the cross-slipping feature were marked by shorter arrow in Fig. 8.8(a).

8.3 Analysis on fracture features during creep

After solution treated at various temperatures, the alloy had different creep properties due to the difference of microstructure as shown in Table 6.2. When solution treated at 1150 °C, the alloy possessed a uniform grain size and wider PPB regions between the grains. Moreover, some coarser γ′ precipitates were distributed along the PPB regions in which no fine γ′-phase was precipitated in the regions near the coarser γ′-phase, as shown in Fig. 4.2(a), the regions possessed a lower creep strength due to the cause of the γ′-free phase zone. After the alloy was solution treated at 1160 °C and twice aged, the coarser γ′ precipitates along the boundary regions disappeared, the boundaries appeared obviously in between the grains. And the cohesive strength between the grains was obviously improved due to the pinning effect of the fine carbide particles, as shown in Fig. 4.3(b), therefore, the alloy displayed a better creep resistance and longer the lifetime.

After the 1120 °C HIP alloy was solution treated at 1160 °C and twice aged, the alloy was crept for 104 h up to fracture under the applied stress of 1034 MPa at 650 °C, the fracture after the alloy was crept up to rupture displayed the initiating and propagating feature of the cuneiform crack as marked by letters A and B in Fig. 8.3. The schematic diagram of the crack initiated along the triangle boundary is shown in Fig. 8.9, where σ_n is the normal stress applied on the boundary, L is the boundary length, h is the displacement of the cuneiform crack opening, α is the crack length, θ is the inclined angle of the adjacent boundaries.

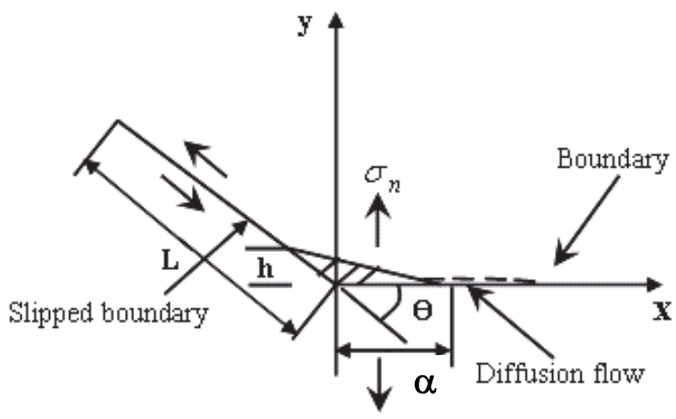

Fig. 8.9. Schematic diagram of the crack initiated along the triangle boundary

Under the action of the applied stress, significant amount of the activated dislocations are piled up the regions near the boundary to bring the stress concentration, which results in the initiation of the crack in the region near the triangle boundary, and the crack is

propagated along the boundary as the creep goes on. Thereinto, the critical length (α_C) of the instable crack propagated along the boundary can be expressed as follows (Yoo M. H., 1983).

$$a_c = \frac{Gh^2}{2\pi(1-\nu)\cdot\gamma_f} \tag{8.1}$$

Where, G is shearing modulus, ν is Poisson ratio, γ_f is the crack propagating work, h is the displacement of the cuneiform crack opening. This indicates that critical length (α_c) of the instable crack propagated along the boundary increases with the displacement of the crack opening, and is inversely to the crack opening work. Thereinto, the displacement of the crack opening increases with the creep time, which can be express as follows:

$$h(t) = \frac{\tau}{\beta}\left[1-\exp(-\frac{4\cdot t\cdot\alpha\cdot\delta_B\cdot\sin\theta}{\pi\eta_B})\right] \tag{8.2}$$

Where $h_w=(\tau/\beta)$ is the max displacement of the crack opening, τ is the resolving shear stress component applied along the boundary, t is the time of the crack propagation, δ_B is the boundary thickness, η_B is the sticking coefficient of the boundary slipping, β is the material constant.

The Eq. (8.2) indicates that the displacement of the crack opening (h) increases with the time and length of crack propagation. When two cuneiform-like cracks on the same boundary are joined each other due to their propagation, the intergranular rupture of the alloy occurs to form the smooth surface on the fracture. The schematic diagram of two cuneiform-like cracks initiated and propagated along the boundary for promoting the occurrence of the intergranular fracture is shown in Fig. 8.10. If the carbide particles are dispersedly precipitated along the boundaries, the ones may restrain the boundaries slipping for improving the creep resistance of the alloy to form the non-smooth surface on the fracture, as marked by arrow in Fig. 8.3(b).

After solution treated at 1165 °C and twice aged, the grain size of the alloy increased obviously, and the carbide films were formed along the boundaries as shown in Fig. 4.4, which weakened the cohesive strength between the grains. Therefore, the cracks were easily initiated and propagated along the boundaries adjoined to the carbide films, which may sharply reduce the lifetime and plasticity of the alloy during creep.

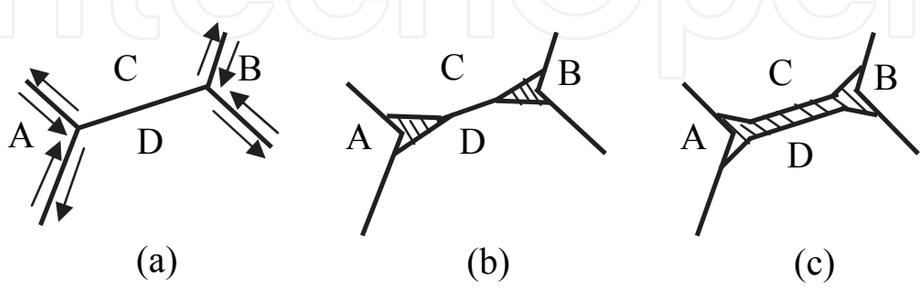

Fig. 8.10. Schematic diagram of the cuneiform-like cracks initiated and propagated along the boundary. (a) Triangle boundary, (b) initiation of the cuneiform-like crack, (c) propagation of the crack along the boundary

Because the boundaries and the carbide particles can effectively hinder the dislocation movement, and especially, the carbide particles can improve the cohesive strength between the grains and restrain the boundaries slipping during creep, therefore, it may be concluded that the carbide particles precipitated along the boundaries have an important effect on improving the creep resistance of the alloy. Although the carbide particles precipitated along the boundaries can improve the strength of the boundaries, the micro-cracks are still initiated and propagated along the boundaries, which suggests that the boundaries are still the weaker regions for causing fracture of the alloy during creep. And once, the carbide is continuously precipitated to form the film along the boundary, which may weaken the cohesive strength between the grains to damage the creep lifetimes of the alloy. The analysis is in agreement with the experimental results stated above.

When the alloy was solution treated at 1150 °C and cooled in oil bath at 120 °C, the carbon atoms were supernaturally dissolved in the matrix of the alloy due to quenching at lower temperature. The concentration supersaturation in the alloy promoted the carbon atoms for precipitating in the form of the fine carbide particles during creep under the applied higher tensile stress at 650 °C, in especially, the slipping trace regions support a bigger extruding stress for inducing the carbon atoms to precipitate in the form of the fine carbide particles along the slipping traces as shown in Fig. 8.7(c). This is thought to be a main reason of the fine carbides precipitated along the slipping traces.

On the other hand, when the alloy was solution treated at 1150 °C and cooled in molten salt at 583 °C, although the slipping traces appeared still in the matrix of the alloy during creep, no fine carbide particles were precipitated along the slipping traces, as shown in Fig. 8.8, due to the concentration supersaturation of the carbon atoms in the matrix is lower than the one of the alloy cooled in oil bath at 120 °C.

9. Conclusion

By means of hot isostatic pressing and heat treated at different temperatures, creep curves measurement and microstructure observation, an investigation had been made into the influence of hot isostatic pressing and heat treatment on the microstructure and creep behaviors of FGH95 nickel-base superalloy. Moreover, the deformation and fracture mechanisms of the alloy were discussed. The conclusions were mainly listed as follows:

1. When the alloy was hot isostatic pressed below the dissolving temperature of γ′ phase, as the HIP temperature increased, the size and amount of primary coarse γ′ phase decreased gradually in the PPB regions, and the size of the grains was equal to the one in the previous powder particles. With the HIP temperature increased to 1180°C, the coarse γ′ phase in the PPB was completely dissolved, and the grain of the alloy grew up obviously.
2. When the solution temperature was lower than the dissolving temperature of γ′ phase, after solution treated at 1140 °C, finer γ′ phase was dispersedly precipitated within the grains, and some coarser γ′ precipitates were distributed in the wider boundary regions where appeared the depleted zone of the fine γ′-phase. With the solution temperature increased, the amounts of the coarser γ′ phase and the zone of γ′-free phase decreased gradually.
3. After solution temperature increased to 1160 °C, the coarser γ′ phase in the alloy was fully dissolved, the fine secondary γ′ phase with high volume fraction was dispersedly

distributed within the grains, and the particles of (Nb, Ti)C carbide were precipitated along the boundaries. When the alloy was solution treated at 1165 °C, the size of the grains was obviously grown up, and the carbides were continuously precipitated to form the films along the boundaries.

4. During long term aging in the ranges of 450 °C and 550 °C, no obvious change in the grain size was detected in the alloy as the aging time prolonged, but the γ′ phase grew up slightly. With the aging time prolonging, the lattice parameters of the γ and γ′ phases increases slightly, but the misfit of γ γ′ phases decreased slightly.
5. Under the applied stress of 1034 MPa at 650 °C, the solution treated alloy cooled in molten salt displayed a better creep resistance. In the ranges of the applied temperatures and stresses, the creep activation energy of the alloy was measured to be Q = 590.3±20 kJ/mol.
6. The deformation mechanisms of the alloy during creep were the twinning, dislocations by-passing or shearing into the γ′ phase. The <110> super-dislocations shearing into the γ′ phase may be decomposed to form the configuration of (1/3)<112> super-Shockleys partial plus stacking fault.
7. During creep, the deformed features of the solution treated alloy cooled in oil bath was that the double orientation slipping of dislocations were activated, and the fine carbide particles were precipitated along the regions of the slipping traces. And the depleted zone of the fine γ′ phase was broken into the irregular piece-like shape due to the severe plastic deformation.
8. The deformed features of the alloy treated in molten salt were that the twinning and dislocation tangles were activated in the matrix of the alloy. Thereinto, the fact that the particles-like carbides were dispersedly precipitated within the grains and along the boundary might effectively restrain the dislocation slipping and hinder the dislocations movement, which is one important factor of the alloy possessing the better creep resistance and the longer creep lifetime.
9. In the later stage of creep, the slipping traces with the single or double orientations features appeared on the surface of the alloy. As the creep went on, the amount of the slipping traces increased to bring about the stress concentration, which might promote the initiation and propagation of the micro-cracks along the boundaries, this was thought to be the main fracture mechanism of the alloy during creep.

10. References

Domingue J. A., Boesch W. J., Radavich J. F.. (1980). S*uperalloys1980*. pp.335 – 344.

Flageolet B.; Jouiad M.; Villechaise P., et al. (2005). *Materials Science and Engineering A*, Vol. 399, pp. 199 – 205, ISSN: 0921 – 5093.

Hirth J. P. & Lothe J. (1968). Theory of Dislocations, 2nd ed., Wiley, New York, p.319

Hu B. F., Chen H. M., Li H. Y., et al. (2003). *Journal of Materials Engineering*, No.1, pp. 6 – 9, ISSN: 1001 – 4381.

Hu B. F., Yi F. Zh., et al. (2006). *Journal of University of Science and Technology Beijing*, Vol.28, No.12, pp. 1121 – 1125, ISSN: 1001 – 053X.

Jia CH. CH., Yin F. ZH., Hu B. F., et al. (2006). *Materials Science and Engineering of Powder Metallurgy*, Vol.11, No.3, pp.176 – 179, ISSN: 1673 – 0224

Klepser C. A.. (1995). Scripta Metallurgical, Vol.33, No.4, pp. 589 – 596, ISSN: 1359 – 6462.

Kovarik L. , Unocic R. R. , Li J. , et al. (2009). *Journal of the Minerals*, Vol. 61, No.2, pp. 42 – 48, ISSN: 1047 – 4838.

Koble M.. (2001). *Materials Science and Engineering A*, Vol. 319-321, PP. 383 – 387, ISSN: 0921 – 5093.

Lherbier L.W. & Kent W. B.. (1990). *The International Journal of Powder Metallurgy*, Vol.26, No.2, pp. 131 – 137, ISBN: 0361 – 3488.

Liu D. M., Zhang Y., P. Liu Y., et al. (2006). *Powder Metallurgy Industry*, Vol.16, No.3 pp. 1-5, ISSN: 1006 – 6543.

Lu Z. Z., Liu C. L., Yue Z. F.. (2005). *Materials Science and Engineering A*, Vol. 395, pp. 153 – 159, ISSN: 0921 – 5093.

Park N. K. & Kim I. S.. (2001). *Journal of Materials Processing Technology*, Vol. 111, No.2, pp. 98 – 102, ISSN: 0924 – 0136.

Paul L.. (1988). *Powder Metallurgy Superalloys*, pp. 27 – 36.

Raujol S., Pettinari F., Locq D., et al. (2004). *Materials Science and Engineering A*, Vol. 387 – 389, pp.678 – 82, ISSN: 0921 – 5093.

Terzi S., Couturier R., Guetal L., et al. (2008). *Materials Science and Engineering A*, Vol. 483-484, pp. 598 – 601, ISSN: 0921 – 5093.

Viswanathan G. B., Sarosi P. M., Henry M. F., et al. (2005). *Acta Materialia*, Vol.53, pp. 3041~3057, ISSN: 1359 – 6454.

Unocic R. R., Viswanathan G. B., Sarosi P. M., et al. (2008). *Materials Science and Engineering A*, Vol. 483 – 484, pp. 25 – 32, ISSN: 0921 – 5093..

Wang P., Dong J. X., Yang L., et al. (2008). Material Review, Vol.22, No.6, pp. 61 – 64, ISSN: 1005 – 023X.

Yoo M. H. & Trinkaus H.. (1983). Metall. Trans., Vol. 14, No.4, pp. 547 – 561, ISSN: 1073-5623.

Zainul H. D.. (2007). *Materials and Design*, Vol.28, pp.1664 – 1667, ISSN: 0261 – 3069.

Zhang J. SH.. (2007). *High Temperature Deformation and Fracture of Material*. Beijing: Science Press, pp. 102 – 105, ISBN: 978 – 7 – 03 – 017774 – 2.

Zhang Y. W., Zhang Y., Zhang F. G., et al. (2002). *Transactions of Materials and Heat Treatment*, Vol.23, No.3, pp. 72 – 75, ISSN: 1009 – 6264.

Zhou J. B., Dong J. X., Xu Zh. Ch., et al. (2002). *Heat Treatment of Metals*, vol.27, No.6, pp.30 – 32. ISSN: 0254 – 6051.

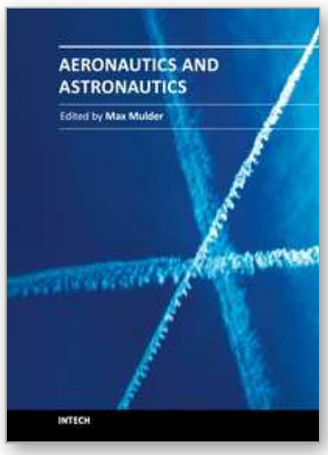

Aeronautics and Astronautics

Edited by Prof. Max Mulder

ISBN 978-953-307-473-3
Hard cover, 610 pages
Publisher InTech
Published online 12, September, 2011
Published in print edition September, 2011

In its first centennial, aerospace has matured from a pioneering activity to an indispensable enabler of our daily life activities. In the next twenty to thirty years, aerospace will face a tremendous challenge - the development of flying objects that do not depend on fossil fuels. The twenty-three chapters in this book capture some of the new technologies and methods that are currently being developed to enable sustainable air transport and space flight. It clearly illustrates the multi-disciplinary character of aerospace engineering, and the fact that the challenges of air transportation and space missions continue to call for the most innovative solutions and daring concepts.

InTech Europe
University Campus STeP Ri
Slavka Krautzeka 83/A
51000 Rijeka, Croatia
Phone: +385 (51) 770 447
Fax: +385 (51) 686 166
www.intechopen.com

InTech China
Unit 405, Office Block, Hotel Equatorial Shanghai
No.65, Yan An Road (West), Shanghai, 200040, China
中国上海市延安西路65号上海国际贵都大饭店办公楼405单元
Phone: +86-21-62489820
Fax: +86-21-62489821

IntechOpen